Department of Physics and Astronomy

Heidelberg University

Master's thesis
in Physics

submitted by
Michael Rautenberg
born in Herdecke, Germany

2021

Theoretical considerations concerning the relation of

the Efimov scenario to Fermi polarons

and upgrade of a polaron experiment

This Master's thesis has been carried out by Michael Rautenberg

at the

Physikalisches Institut

under the supervision of

Prof. Dr. Matthias Weidemüller

Theoretical considerations concerning the relation of the Efimov scenario to Fermi polarons and upgrade of a polaron experiment:

In the first part of this thesis the scenario of two heavy bosons immersed in a Fermi sea is investigated theoretically in the framework of Born-Oppenheimer approximation. The bound state spectrum is discussed as a function of both inter- and intraspecies interactions as well as the fermion density, also including the zero density limit where the system recovers the three-body Efimov spectrum. The modifications of the Efimov scaling law in the presence of a Fermi sea and deviations due to the underlying boson-boson Van der Waals interactions are investigated numerically for the ^{6}Li-^{133}Cs system. Additionally, we find resonances in the induced boson-boson scattering length at the positions where the in-medium Efimov states cross the continuum threshold. For sufficiently large mass ratio quasibound states are formed.

The second part focusses on the improved creation of a Bose-Einstein condensate (BEC) of ^{133}Cs at $900\,\mathrm{G}$ that is compatible with the mixing of ^{6}Li at ultracold temperatures, aiming at studying Bose polaron physics. Magnetic field switching times are improved to $\lesssim 1\,\mathrm{ms}$ enabling the creation of a BEC of $\sim 1 \times 10^4$ atoms. A numerical model for the 'dimple trick' is derived, experimentally tested, yielding a phase space density gain of ~ 4 in the current setup and applied to suggest optimizations beyond this. Forced evaporation in different settings is numerically modelled and compared to the experiment.

Theoretische Überlegungen zur Beziehung des Efimov-Szenarios zu Fermi-Polaronen und Ausbau eines Polaronexperiments:

Im ersten Teil dieser Arbeit wird das Szenario zweier schwerer Bosonen in einem Fermi-See theoretisch im Rahmen der Born-Oppenheimer-Näherung untersucht. Das Spektrum der gebundenen Zustände wird als Funktion der Wechselwirkungen zwischen den Spezies und innerhalb der Spezies sowie der Fermionendichte diskutiert, einschließlich des Grenzfalls verschwindender Dichte, in dem das System das Dreikörper-Efimov-Spektrum annimmt. Die Modifikationen des Efimov-Skalierungsgesetzes in Anwesenheit eines Fermi-Sees und Abweichungen davon aufgrund der zugrundeliegenden Boson-Boson Van-der-Waals-Wechselwirkungen werden numerisch für das ^{6}Li-^{133}Cs-System untersucht. Zusätzlich finden wir Resonanzen in der induzierten Boson-Boson-Streulänge an den Positionen, an denen die in-Medium Efimov-Zustände die Schwelle zum Kontinuum der Streuzustände überschreiten. Für hinreichend große Massenverhältnisse bilden sich dort zudem quasigebundene Zustände.

Der zweite Teil konzentriert sich auf die verbesserte Erzeugung eines Bose-Einstein-Kondensats (BEC) von ^{133}Cs bei $900\,\mathrm{G}$, die mit dem Mischen von ^{6}Li bei ultrakalten Temperaturen kompatibel ist und letztlich auf die Untersuchung der Bose-Polaron-Physik zielt. Verbesserte Magnetfeld-Schaltzeiten von $\lesssim 1\,\mathrm{ms}$ ermöglichen ein BEC von $\sim 1 \times 10^4$ Atomen. Ein numerisches Modell für den 'Dimple-Trick' wird aufgestellt und experimentell getestet, was im derzeitigen Experiment einen Phasenraumdichte-Gewinn von ~ 4 ergibt. Das Model wird angewendet, um Optimierungen am experimentellen Aufbau vorzuschlagen. Forcierte Evaporation für verschiedenen Szenarien wird numerisch modelliert und mit dem Experiment verglichen.

Contents

1 Introduction

Quantum mechanics today is one of the most powerful and well tested fundamental theories of physics. Despite this, its direct application is quite limited to microscopic systems consisting of only a few particles because - even with the numerical computation capacities of modern information processing - the exponentially growing Hilbert space prohibits the exact solution of systems comprised of more than a few tens of (fermionic) constituents. This effectively prevents the description of the properties even of mesoscopic - let alone macroscopic - systems in a bottom up approach which relies on the exact solution of the underlying quantum mechanical description of reality. This is why, since the very early days of the advent of quantum mechanics, effective theories were formulated trying to connect quantum and classical regimes. One of these very useful concepts describing emergent phenomena in terms of so-called quasiparticles in the context of solid state physics is the polaron. Originally describing an electron travelling through a lattice dressed by phononic excitations (Landau and Pekar 1948; Fröhlich 1954), nowadays any type of dressed impurity can be denoted Fermi or Bose polaron depending on the quantum statistics of the bath it is immersed in.

Although extensively studied, the theoretical description of polaronic systems is very challenging, as simple perturbative or mean-field approaches are often not capable of capturing the relevant physics. Especially for mobile impurities in more than one-dimensional systems, often no analytical solution exists and one has to rely on sophisticated numerical methods such as diagrammatic Monte Carlo simulations. A recent overview of the theoretical work an Fermi and Bose polarons can be found in Schmidt et al. 2018 and Grusdt and Demler 2015, respectively.

As inherently many-body quantum mechanical systems, these problems are in general hard to tackle from a theoretical and numerical point of view, while considering also interactions between multiple polarons makes things even more complicated. Nevertheless, in some limiting cases these problems can be solved in good approximation. In the first part of this thesis (chapter 2) I will investigate one of these limits, the one of large mass imbalance: In this case the system of interest consists of two heavy bosons that are immersed in a sea of light fermions. In this scenario - and for sufficiently large mass ratio - the Born-Oppenheimer approximation can be applied. Interestingly, we will see that the Fermi polaron as a true many-body problem is closely related to the three-body heteronuclear Efimov effect which is recovered by taking the zero-density limit in the Fermi polaron scenario.

There is of course another possible approach to solving inherently complicated quantum many-body problems: Following Feynman's assertion that a simulator intended to model a quantum system should itself be quantum (Feynman 1982), one

can use a well controlled quantum system as a platform to model a given scenario. While we are still lacking a versatile, general purpose 'digital' quantum computer, ultracold gas experiments have demonstrated their power as 'analogue' quantum simulators for many-body problems at least throughout the past two decades (Bloch et al. 2008). To investigate polaron physics, first single-species fermionic systems were successfully applied, see e.g. Nascimbène et al. 2009; Schirotzek et al. 2009; Koschorreck et al. 2012. More recently, mixtures of different atomic species have been used to investigate both Fermi (Kohstall et al. 2012; Cetina et al. 2016) and Bose polarons (Scelle et al. 2013; Jørgensen et al. 2016; Hu et al. 2016; DeSalvo et al. 2019; Yan et al. 2020).

Originally starting from a different context, an experiment was built in Heidelberg aiming at the investigation of a mixture of fermionic Lithium and bosonic Caesium. This experiment has been successfully used to study the heteronuclear Efimov effect in a highly mass-imbalanced system (Pires et al. 2014; Ulmanis et al. 2016; Häfner et al. 2017). Following up on these studies, interesting connections between the Efimov scenario and the Fermi polaron have been found (Sun and Cui 2019) setting the current course to study polaron physics, which requires to cool the atoms to lower temperatures and higher densities until quantum degeneracy is reached. Contributing to the experimental work along these lines, in the second part of this thesis (chapter 3) various technological aspects are considered in an effort to create a Bose-Einstein condensate of Caesium atoms in a way that at the same time allows for the preparation and cooling of Lithium. Ultimately this is intended to produce a degenerate sample of both species - an ideal platform to investigate both Fermi and Bose polarons (Sun, Zhai, et al. 2017; Sun and Cui 2019).

2 From Efimov Scenario to Fermi Polarons

The heteronuclear Efimov effect and polaron physics are related phenomena, even though their connection might at first glance not be obvious. Efimov studied a system of three particles, whereas a polaron is a true many-body state. Still, in the context of ultracold atoms, the underlying interactions are the same (pairwise s-wave) and both effects arise due to an emergent potential between two particles: In the case of the heteronuclear Efimov system the effective potential between the two identical particles is mediated by the distinguishable, third particle whereas in the case of the Fermi polaron the effective potential between two impurities is mediated collectively by the entire Fermi sea. In this sense the interactions of two bosons immersed in a Fermi sea and a heteronuclear Efimov system comprised of two bosons and one fermion only differ in the number of fermions that participate in mediating the potential between the two bosons.

Because of this, the connection of the two effects also becomes apparent by considering a possible experiment using an ultracold mixture of two atomic species: To observe signatures of a (Fermi) polaron, one would need to immerse impurities in a (fermionic) bath, that is cooled to quantum degeneracy. At temperatures above degeneracy, i.e. when the impurities are immersed in a thermal bath, there are no collective excitations, which means that the involved physics would not be considered 'many-body' and one would not talk about polarons in this case. But, in the right regime concerning the relative densities of both species, this scenario can be described as a three-body problem: This system - close to interspecies resonance - exhibits certain peculiarities that go by the name of heteronuclear Efimov effect.

The Efimov effect is by now a well known phenomenon and although originally studied in a very different context (Efimov 1970), could experimentally only be observed thanks to the advent of ultracold atom experiments, cf. Kraemer et al. 2006. In fact, our group's Lithium-Caesium experiment has been used to measure three consecutive Efimov resonances in exactly the configuration mentioned above: by cooling down a Lithium-Caesium mixture to low temperatures[1] that are still above quantum degeneracy, cf. Ulmanis et al. 2016; Ulmanis 2017.

Efimov noticed that in a three-body system (which in our case consists of two identical and one distinguishable particles), assuming only resonant two-body interactions, one obtains an effective attractive potential between the identical particles that is proportional to one over their distance[2] squared. This kind of potential then gives rise to the peculiarities of the Efimov effect (cf. fig. 2.1): an infinite progression

---

[1]Sufficiently low temperatures are needed to suppress higher order partial wave scattering as well as to reach a regime where the thermal wave length is large compared to all relevant length scales.

[2]actually, in hyperradial coordinates the potential is proportional to $1/R^2$, where R is the hyper-
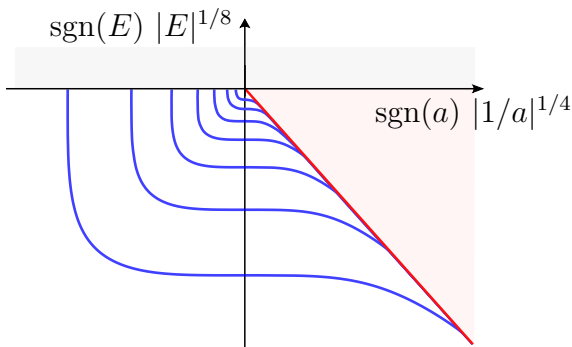
Fig. 2.1: Schematic representation of the energy spectrum in the hetero-nuclear Efimov scenario for two identical bosons and one distinguishable particle. Shown is the energy versus the inverse inter-species scattering length. The energy is rescaled such that the dimer energy $E_b = 1/2\mu a^2$ appears as a straight line (red), to which all Efimov trimers (blue) converge as $1/a$ is increased.

of three-body bound states - for $a < 0$ in a region where the system does not even support two-body bound states - that follow the discrete scaling law

$$a_-^{(n+1)} = \lambda a_-^{(n)} , \qquad a_+^{(n+1)} = \lambda a_+^{(n)} , \qquad E_{n+1} = E_n/\lambda^2 . \qquad (2.1)$$

Here, $a_-^{(n)}$ marks the n-th resonance position where the Efimov trimers cross the three-body continuum (grey shaded area in fig. 2.1) at negative scattering length. Similarly, $a_+^{(n)}$ marks the n-th resonance position where the Efimov trimers cross the dimer plus atom threshold (red line, the red shaded area marks the dimer plus atom continuum) at positive scattering length and E_n is the n-th energy level at resonance ($1/a = 0$). The Efimov states are labelled by non-negative integers $n = 0, 1, 2, \ldots$ The scaling factor $\lambda = e^{\pi/s_0}$, as well as the dimensionless parameter s_0, depend only on the mass ratio, the number of resonant interactions and the quantum statistics of the identical particles. These results can be obtained using hyperspherical coordinates (see e.g. Naidon and Endo 2017) where for the mass ratio of ^{6}Li and ^{133}Cs $M/m \approx 22$ one obtains $s_0 \approx 1.98$ and $\lambda \approx 4.9$ (Ulmanis 2017). The large mass ratio will permit the application of the Born-Oppenheimer approximation (BOA), which accordingly will be used throughout this work. In BOA we find $s_0^{\text{BOA}} \approx 1.82$ and hence $\lambda^{\text{BOA}} \approx 5.6$ which already shows, that the Born-Oppenheimer approximation for the mass ratio of Lithium and Caesium is not yet exact, however, as we will see in chap. 2.2, it captures all the interesting aspects of the Efimov effect.

Starting from this background, we want to make a connection to polaron physics which in this setting naturally arises by lowering the temperature of the bath until reaching quantum degeneracy. In order to get a clear idea of the new phenomena that we should expect, in these theoretical considerations we go to the extreme case of zero temperature, where the problem in Born-Oppenheimer approximation becomes well tractable. We expect the results to hold also at typical temperatures

---

radius, cf. Naidon and Endo 2017. In Born-Oppenheimer approximation we will work directly with coordinates where the effective potential will be a function of the distance of the two identical particles, justifying the interpretation above.

in ultracold gas experiments that are normally of the order of a few percent of the Fermi temperature.

Summing this up, we want to consider the following system: A few[3] bosonic particles with mass M are immersed in a (large) sample of a degenerate Fermi gas made of light fermions with mass $m \ll M$. Although the discussion is not limited to this case, we will use the masses of ^{133}Cs impurities immersed in a Fermi sea made of light ^{6}Li for all numerical calculations. In the context of ultracold gases all microscopic interactions are well modelled by contact potentials including only two-body s-wave interactions. As we consider the degenerate Fermi gas at zero temperature, the relevant interactions are the ones between fermions and bosons as well as the one between the two bosons, both parametrized by their s-wave scattering length a (sometimes explicitly written as a_{LiCs}) and a_{CsCs}, respectively. Both scattering lengths can be controlled experimentally by the same external magnetic field and are therefore not independent. However, for the following theoretical investigations they are considered as such. The last free parameter that we need to consider is the fermion density, conveniently parametrized by the Fermi momentum k_{F}. In the zero density limit of $k_{\mathrm{F}} \to 0$ we recover the original three-body Efimov effect as we will see below.

The zero temperature effective fermion potential has already been studied by Nishida 2009 and some results concerning the Lithium-Caesium system were already discussed in Sun and Cui 2019. In this work we will additionally include the experimentally relevant Caesium-Caesium Van der Waals interaction, which - for the pure three-body Efimov effect - has been discussed e.g. in Ulmanis 2017.

This theory part is structured as follows: After revising the fermion-mediated potential derived in Nishida 2009 (sec. 2.1) and bringing it into a form suited for further calculations (sec. 2.1.1), I will shortly go through the steps of the Born-Oppenheimer approximation also including the Caesium-Caesium interactions (sec. 2.1.2). Then we have everything that we need to solve the Schrödinger equation for bound states and investigate the modified energy spectrum in chap. 2.2 as well as the modified scattering properties of the two heavy bosons in chap. 2.3.

---

[3]'a few' bosons here means that the boson density is low enough that we can neglect the situation in which three bosons come sufficiently close to alter the two-boson-formalism that we are going to employ. Hence, we are back to an effective three-'body' problem: two bosons and a Fermi sea.

2.1 Born-Oppenheimer approximation and fermion-mediated potential

Considering two heavy bosons of mass M immersed in a bath of fermions with mass $m \ll M$, all quantities of interest can be computed by solving the Schrödinger equation

$$H\Psi\left(\{\mathbf{r}_j\},\mathbf{R}\right) = E\Psi\left(\{\mathbf{r}_j\},\mathbf{R}\right) \tag{2.2}$$

for the many-body wave function Ψ that depends on all fermion coordinates $\{\mathbf{r}_j\}$ as well as on the separation vector between the two bosons $\mathbf{R}$. The Hamiltonian, assuming non-interacting fermions, is given by ($\hbar = 1$ throughout this chapter)

$$H = -\frac{\nabla_{\mathbf{R}}^2}{M} - \sum_{j=1}^N \frac{\nabla_{\mathbf{r}_j}^2}{2m} + V_{\mathrm{vdW}}(R) + \sum_{j=1}^N \left[V_{BF}\left(\left|\mathbf{r}_j + \frac{\mathbf{R}}{2}\right|\right) + V_{BF}\left(\left|\mathbf{r}_j - \frac{\mathbf{R}}{2}\right|\right) \right] \tag{2.3}$$

where the coordinate system has been chosen such that the centre of mass of the two bosons lies in the origin, i.e. the bosons are located at $\mathbf{R}_{1,2} = \pm\mathbf{R}/2$. The boson-boson Van der Waals interaction is given by V_{vdW}, see sec. 2.1.2 and the bosons interact with the fermions through V_{BF}, see sec. 2.1.1. When the number of fermions N is decreased until $N = 1$, eq. (2.3) recovers the form of the three-body Hamiltonian used to study the heteronuclear Efimov effect, cf. Ulmanis 2017.

The problem becomes tractable by using the Born-Oppenheimer approximation (BOA) that can be applied here thanks to the large mass ratio $M/m \gg 1$, becoming exact for $M/m \to \infty$. This allows the use of a product ansatz for the wave function and conceptionally follows two steps: First, the Schrödinger equation is solved for the fast degrees of freedom, in our case the light fermions, keeping the heavy bosons fixed. One obtains an effective potential that only parametrically depends on the positions of the two bosons that in the centre of mass frame only depends on their distance $R = |\mathbf{R}_1 - \mathbf{R}_2|$. For zero temperature, this has been done in Nishida 2009. In the second step, the Schrödinger equation for the slow degrees of freedom is solved yielding e.g. the bounds states of the system (see sec. 2.2).

Denoting the (many-body) fermion wave function by $\psi_{\mathrm{R}}\left(\{\mathbf{r}_j\}\right)$ depending on the distance R between the bosons only parametrically and the boson wave function by $\Phi(\mathbf{R})$, the ansatz wave function has the separable form

$$\Psi\left(\{\mathbf{r}_j\},\mathbf{R}\right) = \psi_{\mathbf{R}}\left(\{\mathbf{r}_j\}\right)\Phi(\mathbf{R}) \quad . \tag{2.4}$$

With this notation, the first step of BOA is to solve

$$H_{BF}\,\psi_{\mathrm{R}}\left(\{\mathbf{r}_j\}\right) = E_{\mathrm{eff}}(R)\,\psi_{\mathrm{R}}\left(\{\mathbf{r}_j\}\right) \tag{2.5}$$

where the Hamiltonian H_{BF} contains only the kinetic terms for the fermions as well as the fermion-boson interactions of the full Hamiltonian in eq. (2.3).

Before performing the second step of the Born-Oppenheimer approximation, which consists in solving

$$\left[-\frac{\nabla_{\mathbf{R}}^2}{M} + E_{\text{eff}}(R) + V_{\text{vdW}}(R) \right] \Phi(\mathbf{R}) = E\ \Phi(\mathbf{R}) \tag{2.6}$$

and will be discussed in more detail in sec. 2.1.2, we will first have a closer look at the fermion-mediated potential and rewrite it in a dimensionless form suited for further calculations.

2.1.1 Effective fermion-mediated potential

Closely following Nishida 2009, in order to solve eq. (2.5), we consider the wave function $\psi(\mathbf{r})$ of a single light fermion at position $\mathbf{r}$ interacting with two heavy impurities fixed at $\mathbf{R}_1$ and $\mathbf{R}_2$. Instead of giving an explicit form of the attractive short-range potential V_{BF}, the boson-fermion interaction is taken into account by imposing the Bethe-Peierls boundary conditions

$$\psi(\mathbf{r} \to \mathbf{R}_i) \propto \frac{1}{|\mathbf{r} - \mathbf{R}_i|} - \frac{1}{a} + O(|\mathbf{r} - \mathbf{R}_i|) \tag{2.7}$$

where a is the interspecies s-wave scattering length. Solving the free Schrödinger equation for each fermion wave function subject to the boundary conditions eq. (2.7) yields potentially two bound states with energies $E_\pm = -\kappa_\pm^2/2m < 0$ where

$$\kappa_\pm = \frac{1}{a} + \frac{W\left(\pm e^{-R/a}\right)}{R} > 0\ . \tag{2.8}$$

Here, W is the Lambert W function that solves $x = W(x)e^{W(x)}$ which has real solutions for $x \in (-1/e, \infty)$. Hence, the bound state with energy $E_\pm$ exists only for distances $R/a > \mp 1$.

Aside from the bound states, there is a continuum of scattering states with energy $E = k^2/2m > 0$, for each mode k parametrized by an s-wave phase shift $0 \le \delta_\pm(k) \le \pi$ with respect to the free wave function (without impurities) given by

$$\tan\delta_\pm(k) = -\frac{kR \pm \sin(kR)}{R/a \pm \cos(kR)} \tag{2.9}$$

for the symmetric $(+)$ and antisymmetric $(-)$ wave function, respectively. In the thermodynamic limit, i.e. for an infinite number of fermions $N \to \infty$, keeping their density and thus also the Fermi momentum k_{F} fixed, one can show that the total energy of the system changes with respect to the case without impurities by

$$E_{\text{eff}}(R) = -\frac{\kappa_+^2 + \kappa_-^2}{2m} - \int_0^{k_{\text{F}}} dk\ k\ \frac{\delta_+(k) + \delta_-(k)}{\pi m}\ . \tag{2.10}$$

This result was derived by Nishida 2009 for the case of two heavy fermions immersed in a Fermi sea of light fermions but also holds for bosonic impurities. In

eq. (2.10) all length scales can be conveniently expressed in terms of the (inverse) Fermi momentum k_F by introducing the Fermi energy $E_\text{F} = k_\text{F}^2/2m$ as a reference scale. Because including the boson-boson Van der Waals interaction naturally introduces a new length scale (the boson-boson Van der Waals length r_vdW as we shall see below), we first want to write the effective potential (as well as the whole Schrödinger equation) in a dimensionless form using some length scale r_0. This can be done for arbitrary length scales $r_0 \neq 0$, but in the end we will set $r_0 \equiv r_\text{vdW}$.

That is, we define a dimensionless distance between the two bosons $\hat{R} \equiv R/r_0$, a dimensionless interspecies scattering length $\hat{a} \equiv a/r_0$ and a dimensionless Fermi momentum $\hat{k}_F \equiv k_F\,r_0$. Then the effective potential $\epsilon_\text{eff} \equiv E_\text{eff}/E_0$ (in terms of the reference energy $E_0 \equiv 1/mr_0^2$) reads

$$\epsilon_\text{eff}(\hat{R}, \hat{a}, \hat{k}_F) = -\frac{\kappa_+^2(\hat{R}, \hat{a}) + \kappa_-^2(\hat{R}, \hat{a})}{2} - \int_0^{\hat{k}_F} dx\, x \frac{\delta_+(x, \hat{R}, \hat{a}) + \delta_-(x, \hat{R}, \hat{a})}{\pi} \quad (2.11)$$

where the momenta corresponding to the bound state contributions are given by

$$\kappa_\pm(\hat{R}, \hat{a}) = \frac{1}{\hat{a}} + \frac{W\left(\pm \exp\left(-\hat{R}/\hat{a}\right)\right)}{\hat{R}} \quad (2.12)$$

and the scattering phase shifts are

$$\delta_\pm(x, \hat{R}, \hat{a}) = \arctan\left[-\frac{x\hat{R} \pm \sin(x\hat{R})}{\frac{\hat{R}}{\hat{a}} \pm \cos(x\hat{R})}\right]\,. \quad (2.13)$$

Here, the arctan is defined such that again $0 \leq \delta_\pm \leq \pi$.

Later, we will be interested in the energy *difference* compared to the situation where two infinitely separated, thus non-interacting, bosons are immersed in the Fermi gas, hence we need $\epsilon_\infty = \epsilon_\text{eff}(\hat{R} \to \infty)$. This can be calculated analytically as

$$\epsilon_\infty(\hat{a}, \hat{k}_F) = -\Theta(\hat{a})\,\frac{1}{\hat{a}^2} - \frac{1}{\pi}\left[-\frac{1}{\hat{a}^2}\tilde{\arctan}(\hat{k}_F\hat{a}) + \hat{k}_F\left(\frac{1}{\hat{a}} + \hat{k}_F\,\arctan(-\hat{k}_F\hat{a})\right)\right] \quad (2.14)$$

where $\Theta(x)$ denotes the Heaviside step function (being 1 for $x > 0$, else 0) and $\tilde{\arctan}$ is the inverse tangent function with the usual branch cut, i.e. evaluating to values between $-\pi/2$ and $\pi/2$.

With these definitions at hand, we define the dimensionless potential $v_\text{eff} \equiv \epsilon_\text{eff} - \epsilon_\infty$ relative to the case of non-interacting impurities. This potential is shown in fig. 2.2 for different interspecies scattering lengths and fermion densities. In the case of resonant interactions ($1/a = 0$) and vanishing fermion density ($k_\text{F} = 0$) the potential recovers the $\propto 1/R^2$ form that leads to the peculiarities of the Efimov effect. Especially from the right panel it is obvious that the fermionic medium induces an oscillatory behaviour (similar to Casimir or RKKY interactions, see Nishida 2009),
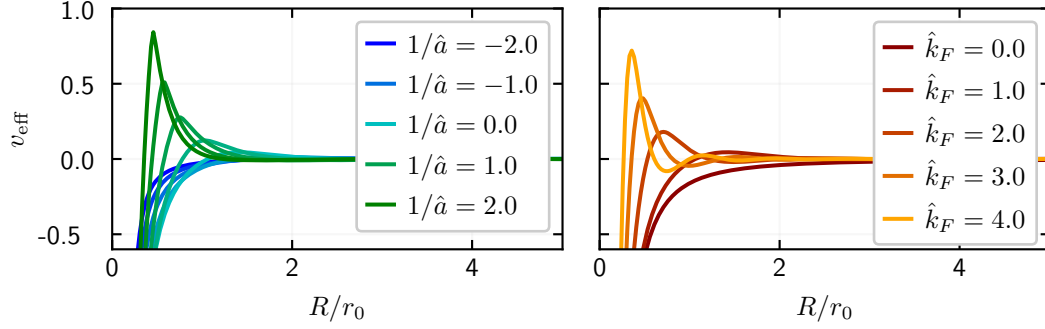
Fig. 2.2: Fermion-mediated potential for different inter-species scattering length $\hat{a}$, for $\hat{k}_{\mathrm{F}} = 1$ (left) and different fermion densities parametrized by Fermi momenta $\hat{k}_{\mathrm{F}}$ for $1/\hat{a} = 0$ (right). Note that these plots are only meant to give an overview over the functional dependence of the induced potential, for a plot with realistic fermion densities, also including the Van der Waals interaction, see fig. 2.7.

starting with a first 'repulsive barrier' around $\hat{R} \approx 1/\hat{k}_{\mathrm{F}}$. As we will see later on, this barrier will alter the Efimov scaling law, eq. (2.1), further, it will have an influence on the range where this modified scaling law can be observed and will also allow for the formation of quasibound states at positive energies (given a sufficiently large mass ration M/m) which influences the induced scattering properties of the heavy impurities.

2.1.2 Schrödinger equation in BOA including boson-boson interaction

Now that we have the effective potential in a suitable form, we want to complete the last step of the BOA and solve the Schrödinger equation for the slow degrees of freedom, here also including the boson-boson Van der Waals interaction.

To this end we set the arbitrary length scale r_0 introduced in sec. 2.1.1 to the Van der Waals length $r_0 = r_{\mathrm{vdW}}$. This is the natural choice of reference scale which becomes evident when including the boson-boson Van der Waals potential that we model in the following way (Gribakin and Flambaum 1993):

$$V_{\mathrm{vdW}}(R) = \begin{cases} \infty, & R < R_0 \\ -C_6/R^6, & R > R_0 \end{cases} \tag{2.15}$$

where C_6 is connected to r_{vdW} by (cf. Chin et al. 2010)

$$r_{\mathrm{vdW}} = \frac{1}{2}\left(MC_6\right)^{1/4} \quad . \tag{2.16}$$

Using $E_{\mathrm{vdW}} \equiv 1/Mr_{\mathrm{vdW}}^2$ this means that $C_6 = 2^4 r_{\mathrm{vdW}}^6 E_{\mathrm{vdW}}$.

Starting again with the Schrödinger equation for the slow degrees of freedom, which is now effectively one-dimensional as both E_{eff} and V_{vdW} only depend on $R = |\mathbf{R}|$, for $R > R_0$

$$\left[-\frac{\partial_R^2}{M} + E_{\text{eff}}(R) - \frac{C_6}{R^6} \right] \Phi(R) = E\Phi(R) \tag{2.17}$$

again introducing $\hat{R} \equiv R/r_{\text{vdW}}$ as above, we obtain

$$\left[-\partial_{\hat{R}}^2 + \frac{M}{m}\epsilon_{\text{eff}}(\hat{R}) - \frac{2^4}{\hat{R}^6} \right] \Phi(\hat{R}) = \frac{E}{E_{\text{vdW}}}\Phi(\hat{R}) \ . \tag{2.18}$$

As we will often be interested in the energy difference compared to the two bosons being infinitely far away from each other where they have twice the 'single polaron energy' or chemical potential $2E_p \equiv \epsilon_\infty$, we can rewrite the Schrödinger equation as

$$\left[-\partial_{\hat{R}}^2 + \frac{M}{m}v_{\text{eff}}(\hat{R}) - \frac{2^4}{\hat{R}^6} \right] \Phi(\hat{R}) = \frac{\Delta E}{E_{\text{vdW}}}\Phi(\hat{R}) \ . \tag{2.19}$$

Here, we introduced the effective potential relative to twice the single polaron energy $v_{\text{eff}}(\hat{R}) \equiv \epsilon_{\text{eff}}(\hat{R}) - \epsilon_{\text{eff}}(\hat{R} \to \infty)$ and defined the corresponding eigenenergy as $\Delta E = E - 2E_p$, cf. Nishida 2009; Sun and Cui 2019.

The cutoff radius R_0 is connected to the Caesium-Caesium scattering length a_{CsCs} via the transcendental equation

$$\frac{N_{1/4}(2r_{\text{vdW}}^2/R_0^2)}{J_{1/4}(2r_{\text{vdW}}^2/R_0^2)} = 1 - \sqrt{2}\frac{a_{\text{CsCs}}}{r_{\text{vdW}}}\frac{\Gamma(5/4)}{\Gamma(3/4)}, \tag{2.20}$$

taken from Gribakin and Flambaum 1993, where J and N are Bessel functions of first and second kind, respectively. In order to avoid a branch cut of R_0 at $1/a_{\text{CsCs}} = 0$, I rewrite this equation before numerically solving it as

$$\left[1 - \frac{N_{1/4}(2r_{\text{vdW}}^2/R_0^2)}{J_{1/4}(2r_{\text{vdW}}^2/R_0^2)} \right]^{-1} = \frac{1}{\sqrt{2}}\frac{r_{\text{vdW}}}{a_{\text{CsCs}}}\frac{\Gamma(3/4)}{\Gamma(5/4)} \tag{2.21}$$

The equation above has multiple solutions R_0 for any given a_{CsCs}, corresponding to different numbers of deeply bound dimer states supported by the Van der Waals potential. In the following numerical calculations we will typically use the solution corresponding to one deeply bound dimer state, however, the exact number of deeply bound states is irrelevant for the following discussion as it does not significantly affect the higher lying (in-medium) Efimov states, which depend mostly on the long range behaviour of the potential, see Wang et al. 2012.

Before turning to the numerical results obtained by solving the Schrödinger equation (2.18), I want to briefly discuss some aspects concerning the numerical methods used.

Numerical methods

All results in chap. 2.2 are obtained by solving the (one dimensional) Schrödinger equation (2.18) for bound states. In principle, this is a well-known computational problem that can e.g. be solved using the 'matrix Numerov' method as described in Pillai et al. 2012. However, in the case at hand, we face the difficulty that $v_{\text{eff}}(\hat{R})$ has relevant contributions over several orders of magnitude in $\hat{R}$ before approaching zero. It is therefore reasonable to work with an adaption of the original matrix Numerov method on a logarithmic grid, as described in Giannozzi 2014.

The idea behind the matrix Numerov method is to discretize space and represent the kinetic and potential energy operators as matrices over this grid (hence 'matrix' Numerov method). Once all matrices are set up, the problem reduces to finding the eigenvalues and -vectors of a $N \times N$-matrix, where N is the number of grid points. Depending on the details of the matrices, one can either have periodic boundary conditions or force the wave function to vanish at the boundaries, which effectively places the potential of interest in a box with infinitely high walls. As we model the repulsive core of the Van der Waals potential with a hard sphere, see eq. (2.15), we use the latter configuration. In this case we have to make sure that the last grid point is at sufficiently large $\hat{R}$ so that all wave functions of interest are well decayed before reaching the 'wall' at the edge of the grid. This is why the use of a logarithmic grid is necessary (we typically use a grid up to $\hat{R} = 1 \times 10^{10}$). The first grid point (being the first point in space where the wave function can have a non-zero value) is placed such that the wave function vanishes exactly at the short range cutoff $\hat{R}_0$. Note that because the Schrödinger equation (2.18) is missing a factor of 2 compared to the standard one-dimensional Schrödinger equation, we need to correct the potential before applying the matrix Numerov method and afterwards again remove the correction in the results.

2.2 Bound states: modified Efimov spectrum

Parts of this chapter have been published in

In this chapter we want to investigate how the Efimov spectrum is altered when the fermion density is increased, i.e. when the system transitions from the well known three-body Efimov spectrum ($k_F = 0$) to something that has either been called Fermi polaron or - as will be done in this work - in-medium Efimov effect ($k_F > 0$). To this end, we numerically solve the Schrödinger equation eq. (2.18) for bound states. Having in mind an experiment with an ultracold Lithium-Caesium mixture, we will use the mass ratio of these species ($M/m \approx 22.1$) in all of the following calculations.
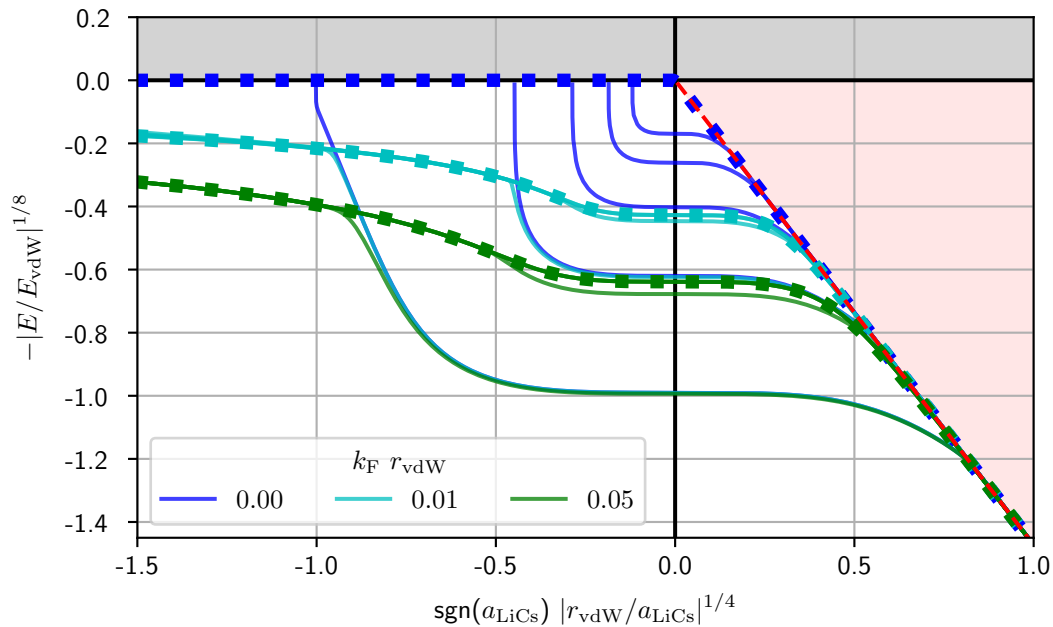

Fig. 2.3: Numerically calculated energy spectrum for different fermion densities (solid lines) as a function of the inverse interspecies scattering length for $a_{CsCs} \to \infty$. The solid squares mark the continuum thresholds $\epsilon_\infty(\hat{a}_{LiCs}, \hat{k}_F)$ for the corresponding values of $\hat{k}_F$. The red shaded area marks the Caesium-Lithium dimer plus Caesium continuum located above the Lithium-Caesium dimer energy (red dashed line) and the grey shaded area marks the three-body continuum. These interpretations strictly only hold for $k_F = 0$.
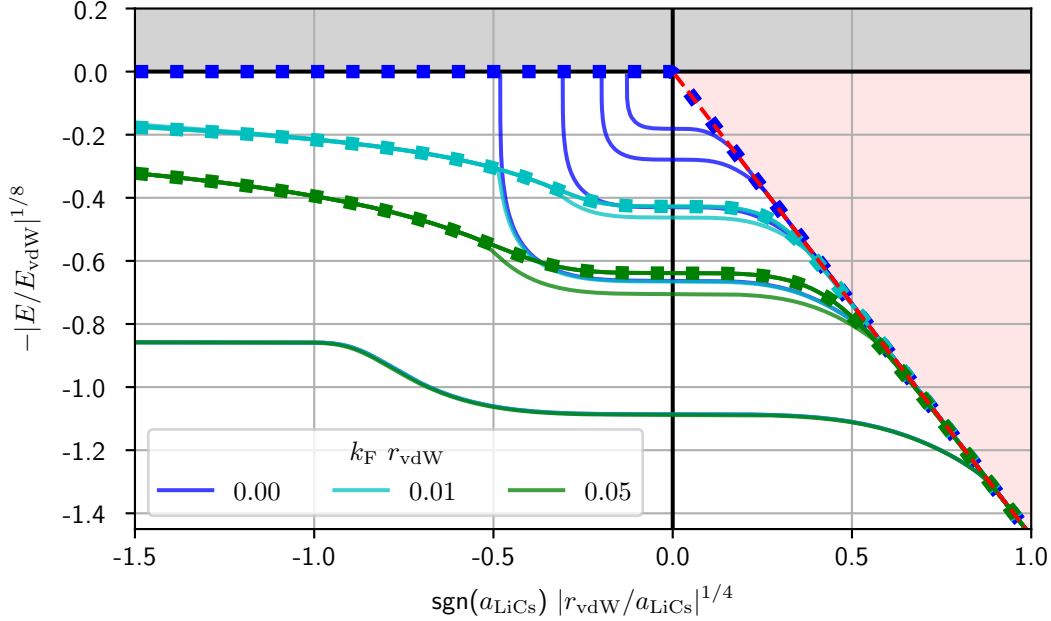
Fig. 2.4: Same spectrum as in fig. 2.3, except here for finite $a_{\mathrm{CsCs}}/r_{\mathrm{vdW}} = 3$. The lowest bound state energy corresponds to a deeply bound Caesium-Caesium dimer.

In fig. 2.3 we calculate the bound state energies for different fermion densities as a function of the inverse interspecies scattering length $1/a_{\mathrm{LiCs}}$. In these calculations we first want to reproduce the Efimov spectrum, i.e we are not interested in the effects introduced by the Caesium-Caesium interactions, hence we set $a_{\mathrm{CsCs}} \to \infty$. The axes have been rescaled in such a way, that the whole spectrum is well visible and additionally the universal Lithium-Caesium dimer energy $E_b \approx -1/ma_{\mathrm{LiCs}}^2$ follows a straight line (shown as a red dashed line delimiting the red shaded area). Starting with the Efimov scenario in vacuum ($k_{\mathrm{F}} = 0$, dark blue lines), we recover the expected spectrum: On the negative scattering length side the trimer energies cross the three-body continuum (grey shaded area) threshold at $E = 0$, whereas for increasing positive scattering length they merge with the Lithium-Caesium dimer state (red dashed line) marking the threshold to the Lithium-Caesium dimer plus Caesium continuum (red shaded area). The dark blue squares mark these thresholds, computed by evaluating $\epsilon_\infty(\hat{a}_{\mathrm{LiCs}}, \hat{k}_{\mathrm{F}})$, see eq. (2.14). We note that for energies $|E/E_{\mathrm{vdW}}|^{1/8} \lesssim 0.1$, i.e. $|E/E_{\mathrm{vdW}}| \lesssim 10^{-8}$ the numerical uncertainties could lead to considerable errors. That is also the reason why only the first four Efimov states are shown (the lowest lying bound state energy corresponds to a deeply bound Caesium dimer, see below). Increasing the fermion density ($k_{\mathrm{F}} > 0$, light blue and green lines) significantly alters the spectrum, especially for negative interspecies scattering length. Although one could still claim that for more and more negative $1/a_{\mathrm{LiCs}}$ the bound state energies merge with the continuum of scattering states, this

continuum threshold (solid squares) is modified by the presence of the Fermi sea. It now describes the situation of two polarons scattering with finite relative momentum where the scattering is (partly) mediated by the fermionic bath.

To further investigate the effects of the Caesium-Caesium scattering length, we compute the same spectrum as above but now for finite $a_{\mathrm{CsCs}}/r_{\mathrm{vdW}} = 3$ being roughly the value that we would expect in the experiment at interspecies resonance, see fig. 2.4. Both spectra look similar, except for the deepest bound state, that we assign to a deeply bound (molecular) Caesium-Caesium dimer state. To see that this is the case, we can e.g. plot the lowest energy eigenstate at some large and negative inverse interspecies scattering length as a function of the Caesium-Caesium scattering length and compare it to $E_{\mathrm{dimer}} = -1/Ma^2$ (i.e. $E_{\mathrm{dimer}}/E_{\mathrm{vdW}} = -(r_{\mathrm{vdW}}/a_{\mathrm{CsCs}})^2$), see fig. 2.5.
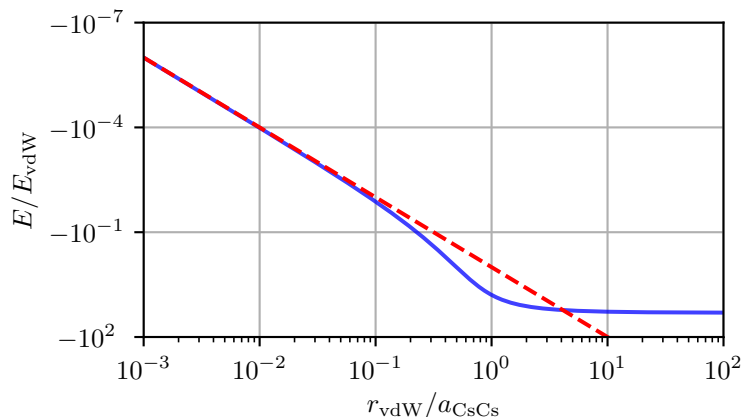

Fig. 2.5: Comparison of the lowest bound state energy for $k_{\mathrm{F}} = 0$ at $r_{\mathrm{vdW}}/a_{\mathrm{LiCs}} = -80$ as a function of the inverse Caesium-Caesium scattering length (solid blue line) and the Caesium-Caesium universal dimer energy $E_{\mathrm{dimer}} = 1/Ma^2$ (red dashed line).

To systematically investigate the effects of the Caesium-Caesium scattering length on the 'Efimov' spectrum for different fermion densities, we now calculate the spectrum as a function of $1/a_{\mathrm{CsCs}}$ at interspecies unitarity ($a_{\mathrm{LiCs}} \to \infty$), i.e. we take a cut through figs. 2.3 and 2.4 at $1/a_{\mathrm{LiCs}} = 0$. The resulting spectra are shown in fig. 2.6.

Shown are again the four lowest Efimov states (labelled $n = 0, \ldots, 3$) and one deeply bound Caesium dimer state in vacuum ($k_{\mathrm{F}} = 0$, dark blue lines). As a function of a_{CsCs} one can see two 'steps' at $|a_{\mathrm{CsCs}}| \approx r_{\mathrm{vdW}}$ that mark the crossover between a Van-der-Waals-dominated ($|a_{\mathrm{CsCs}}| < r_{\mathrm{vdW}}$) dimer to a halo state $|a_{\mathrm{CsCs}}| > r_{\mathrm{vdW}}$, cf. Ulmanis 2017. Comparing this Efimov spectrum (dark blue lines) to the case of two heavy bosons in the presence of a Fermi sea ($k_{\mathrm{F}} > 0$, light blue and green lines) one observes that the in-medium $n \geq 1$ states are less strongly bound compared to the vacuum case until they eventually cross the continuum threshold ($\Delta E \to 0$). This disappearance of the bound states happens earlier (i.e. for deeper
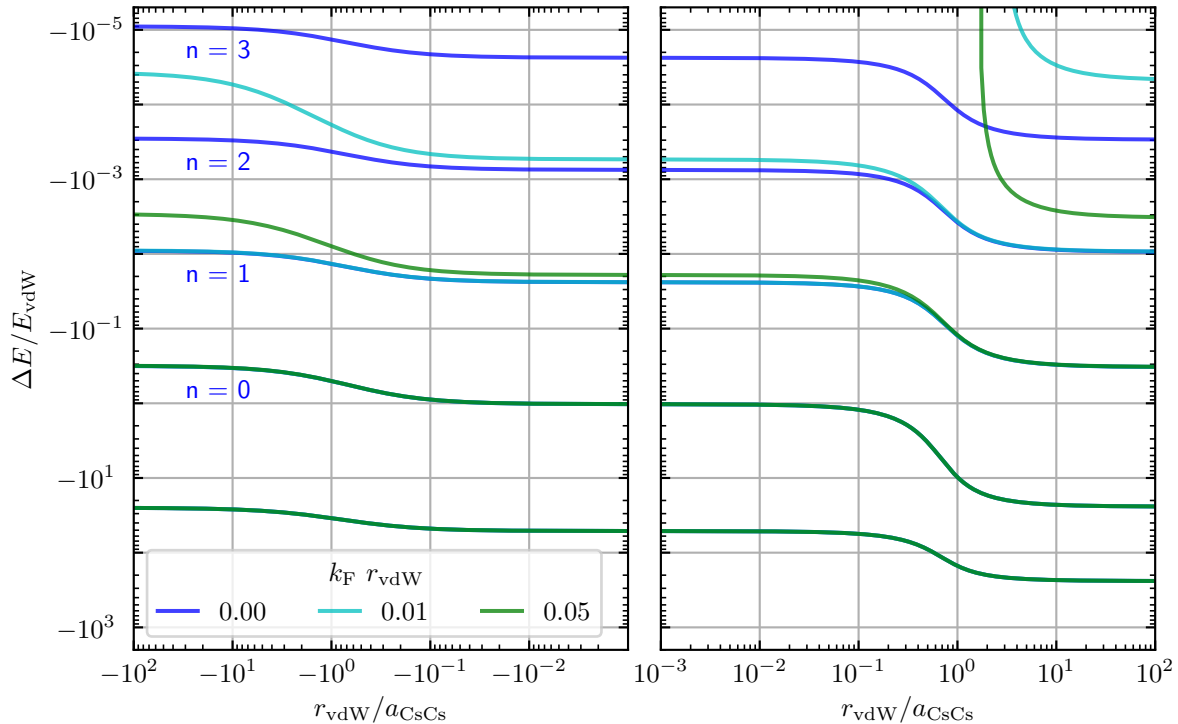
Fig. 2.6: Energy spectrum of two heavy Caesium atoms in the presence of a Fermi sea ($k_F > 0$) compared to the Efimov spectrum in vacuum ($k_F = 0$, dark blue lines). The binding energy is shown relative to the respective continuum threshold (twice the single polaron energy, solid squares in figs. 2.3 and 2.4) as a function of the inverse Caesium-Caesium scattering length.

bound states) the higher the fermion density. At this point we should also point out that the Efimov scaling at $1/a_{CsCs} = 0$ - which manifests itself in equidistant energy lines on this logarithmic plot[4] - breaks down as the fermion density is increased. We will verify below that the scaling law is modified by the presence of the Fermi sea such that the new length scale of the Fermi momentum is also included as has been already pointed out by Nygaard and Zinner 2014 and Sun and Cui 2019.

To understand the suppression of the higher-lying bound states with increasing fermion density, it is instructive to have a closer look at the effective potential as a function of the distance between the two heavy bosons, see fig. 2.7. In the double-logarithmic plot the two contributions to the boson-boson potential are clearly visible: the short range Van der Waals ($\propto 1/R^6$, grey dotted line) and the long range fermion-mediated effective potential ($\propto 1/R^2$, grey dashed line). Increasing the

---

[4]The included Caesium-Caesium Van der Waals potential alters the $1/R^2$ form of the pure Efimov potential such that the Efimov scaling is not strictly fulfilled any more. However, the higher lying states $n \geq 1$, that extend much beyond the short range vdW-dominated regime of the potential (fig. 2.7), follow the Efimov scaling of eq. (2.1) to a very good degree, cf. Ulmanis 2017; Tran et al. 2021.
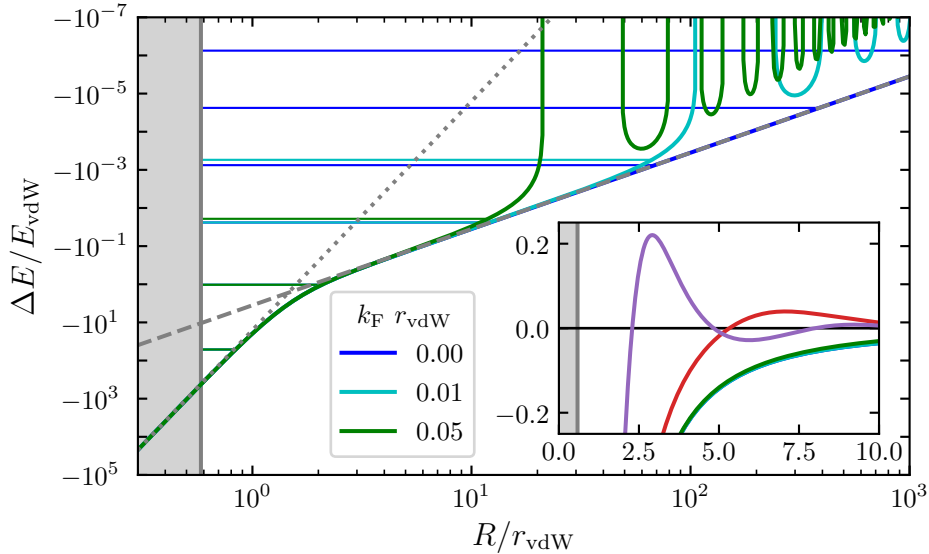
Fig. 2.7: Caesium-Caesium potential for inter- and intraspecies resonance including Van der Waals and fermion-mediated potentials, see eq. (2.18) in vacuum ($k_F = 0$, dark blue) and in the presence of the Fermi sea ($k_F > 0$). To highlight the potential differences for different fermion densities, the negative part of the potential is plotted logarithmically (main panel), an overview for large fermion densities ($\hat{k}_F = 0.2, 0.5$ in red and purple, respectively) is shown linearly in the inset. The grey shaded area marks the region below the cutoff R_0, cf. eq. (2.21), the grey dotted line represents the $2^4/\hat{R}^6$ part of the Van der Waals potential and the grey dashed line marks the $((s_0^{\mathrm{BOA}})^2 + 1/4)/\hat{R}^2$ Efimov part of the potential (in Born-Oppenheimer approximation). The bound state energies corresponding to the different fermion densities are drawn as horizontal lines.

fermion density leaves the short range part unaltered, but introduces an oscillatory behaviour in the long range potential where the first repulsive 'barrier' moves to shorter and shorter distances as the fermion density is increased ($\sim 1/k_F$). This leads to the higher lying bound states (where the corresponding wave functions predominantly explore the long range part of the potential) being less strongly bound, eventually leading to their suppression at high fermion densities. In sec. 2.3 we will see under what conditions a bound state can 'live on' behind this repulsive barrier as a quasibound state at positive energies.

The suppression of the higher-lying bound states can also be directly seen by plotting the spectrum as a function of k_F, see fig. 2.8. This representation is at the same time suited to visualize the (modified) Efimov scaling law. As already mentioned above, adding the Fermi sea alters the pure Efimov scaling law of eq. (2.1) and replaces it by a new scaling law, now also incorporating the new length scale
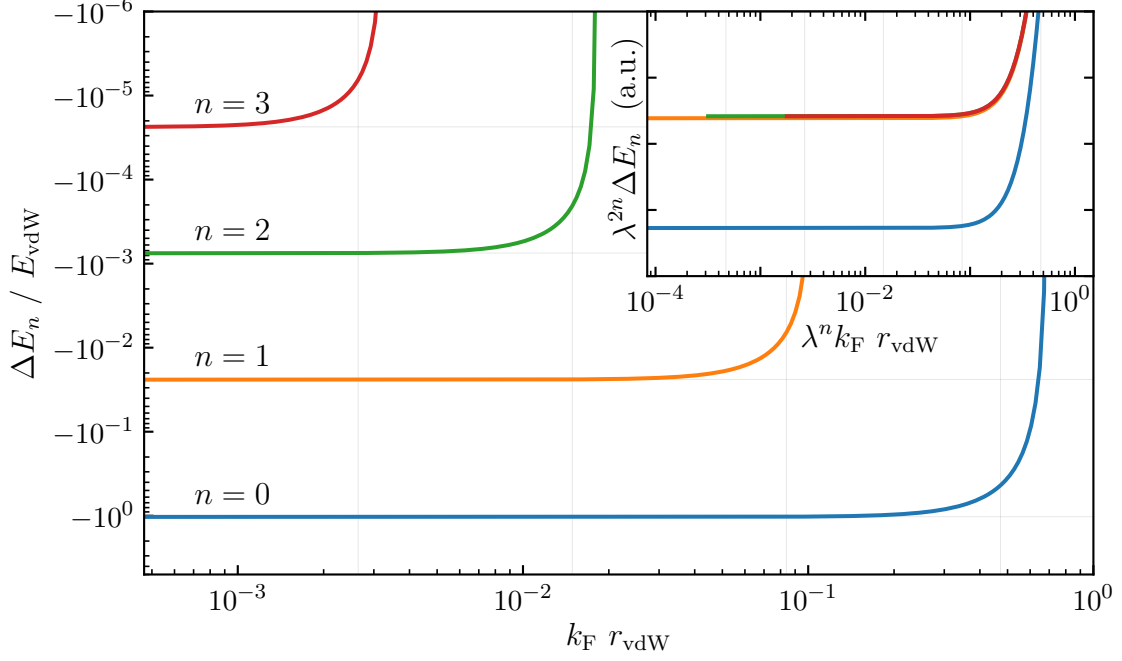
16

Fig. 2.8: Continuous change of the Efimov spectrum with increasing fermion density at inter- and intraspecies resonance. On the very left ($k_F \to 0$) the Efimov spectrum in vacuum is recovered. With increasing fermion density, the less strongly bound states are suppressed one after the other. The inset demonstrates the modified scaling law of eq. (2.22) for $n \geq 1$ (same colour code as in main panel). The lowest lying $n = 0$ state deviates from the scaling law because of the altered short range potential due to the Caesium-Caesium Van der Waals interaction.

$1/k_F$ as pointed out by Sun and Cui 2019:

$$a_-^{(n+1)}(k_F) = \lambda a_-^{(n)}(\lambda k_F) \ , \qquad E_{n+1}(k_F, a) = \lambda^{-2} E_n(\lambda k_F, a/\lambda) \ . \qquad (2.22)$$

When adding the Caesium-Caesium Van der Waals potential, this modified scaling law can be numerically confirmed again only for the higher lying states for the same reasons as above, with very small deviations for the $n = 1$ state, see inset of fig. 2.8.

Having discussed how the bound state spectrum changes under the influence of the Fermi sea, we will now turn to discuss its effect on the scattering properties of two heavy impurities.

2.3 Scattering: resonances and quasibound states

The results discussed in this chapter have been published in

T. Enss, B. Tran, M. Rautenberg, M. Gerken, E. Lippi, M. Drescher, B. Zhu, M. Weidemüller, M. Salmhofer
Scattering of two heavy Fermi polarons: Resonances and quasibound states
Physical Review A **102**, 063321 (2020)

In sec. 2.1.1 we have seen that for positive interspecies scattering length $a > 0$, the fermion-mediated potential develops a repulsive 'barrier', see fig. 2.2 and fig. 2.7. In such a case the question arises whether (or for what parameters) quasibound states can be observed, i.e. meta-stable, positive-energy states that 'live on' behind the barrier and decay on a time scale defined by the resonance width.

The quasibound states appear near the threshold where the in-medium Efimov bound states are 'pushed out' of the potential at the positive scattering length side. As this happens because of the repulsive barrier forming at larger radii ($R \approx 1/k_\mathrm{F}$), this phenomenon is not expected to heavily depend on the Caesium-Caesium interactions which decrease as $1/R^6$. That is why in this chapter - to simplify the following discussion - we will consider a generic case of in-medium Efimov effect, without explicitly including the Caesium-Caesium Van der Waals interaction[5]. Thus, throughout this chapter we will work in Fermi units instead of Van der Waals units as above, i.e. our reference length scale is the (inverse) Fermi momentum $1/k_\mathrm{F}$ and the reference energy is the corresponding Fermi energy $E_\mathrm{F} = k_\mathrm{F}^2/2m$.

Still working in Born-Oppenheimer approximation, in the following we will solve the Schrödinger equation

$$\left[-\frac{\nabla_\mathbf{R}^2}{M} + V(R) + 2\mu - E \right] \Phi(\mathbf{R}) = 0 \tag{2.23}$$

for scattering states with $E > 0$. The central potential $V(R)$ is again the fermion-mediated potential introduced in sec. 2.1.2, in Fermi units given by $V(k_\mathrm{F}R)/E_\mathrm{F} = 2v_\mathrm{eff}(k_\mathrm{F}R, k_\mathrm{F}a)$, which directly follows from setting the arbitrary length scale $r_0 = 1/k_\mathrm{F}$ in sec. 2.1.1. Using Fermi units, the single polaron energy (chemical potential) takes the simpler form, see Nishida 2009

$$\mu/E_\mathrm{F} = -\frac{k_\mathrm{F}a + \left[1 + (k_\mathrm{F}a)^2\right]\left[\pi/2 + \arctan(1/k_\mathrm{F}a)\right]}{\pi(k_\mathrm{F}a)^2} \tag{2.24}$$

---

[5]The repulsive core of the Caesium-Caesium Van der Waals interaction will serve as short range regularization for the singular $1/R^2$ potential, i.e. it will still be included implicitly via the short range cutoff, here serving as the three-body parameter.

as compared to eq. (2.14).

As we want to investigate the scattering properties, we are not interested in the energy E in eq. (2.23), but rather in the scattering phase shifts $\delta_l^{\mathrm{ind}}(k)$ induced by the potential in the l-th partial wave component. Limiting the discussion to the s-wave ($l = 0$) phase shift, this can be calculated by integrating the variable phase equation, cf. Calogero and Green 1968, which in our case reads

$$k\partial_R \delta_{l=0}^{\mathrm{ind}}(k, R) = -MV(R)\sin^2\left[kR + \delta_{l=0}^{\mathrm{ind}}(k, R)\right]. \tag{2.25}$$

Imposing the boundary condition $\delta_{l=0}^{\mathrm{ind}}(k, R = 0) = 0$ and integrating from $R = 0$ to large R one can usually extract the induced scattering phase shift as $\delta_{l=0}^{\mathrm{ind}}(k) = \delta_{l=0}^{\mathrm{ind}}(k, R \to \infty)$.

In the case at hand, however, the potential has a singularity at short distances as it goes as $V(R \to 0) \propto 1/R^2$. The regularization that is needed to circumvent this singularity is physically provided by the repulsive core of the Caesium-Caesium Van der Waals potential, which we model by a hard sphere of radius R_0. In this case the boundary condition is $\delta_{l=0}^{\mathrm{ind}}(k, R = R_0) = -kR_0$, i.e. we include all the short-range scattering details in the phase shift at the cutoff radius, thereby relating R_0 to the three-body parameter, see e.g. Braaten and Hammer 2006. The variable phase equation (2.25) is then integrated[6] from $R = R_0$ to ∞. As we do not explicitly model the Caesium-Caesium interactions, the short range cutoff R_0 needs to be tuned to match experimental results: Using the value of $a_-^{(1)} = -2130\,a_0$ at the Lithium-Caesium Feshbach resonance near $889\,\mathrm{G}$ (Häfner et al. 2017) which is reproduced by our model potential with $R_0 = 220\,a_0$ and typical fermion densities of $n \approx 1 \times 10^{13}\,\mathrm{cm}^{-3}$, we will use $k_{\mathrm{F}}R_0 = 0.1$ in the following discussion.
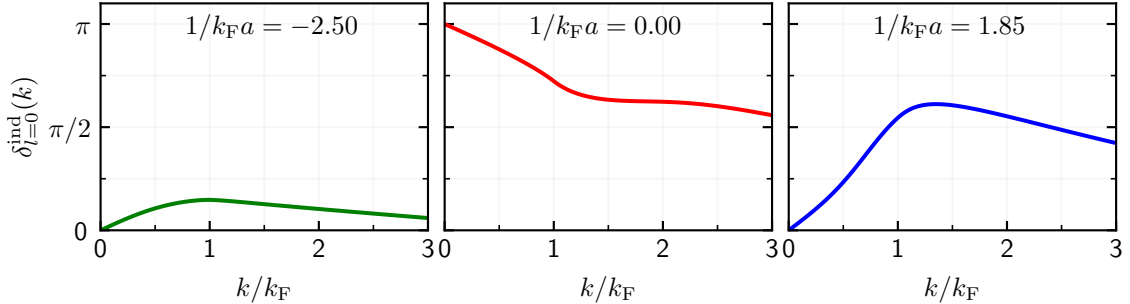

Fig. 2.9: Induced scattering phase shifts $\delta_{l=0}^{\mathrm{ind}}(k)$ for different Lithium-Caesium interactions $1/k_{\mathrm{F}}a$ calculated by numerically integrating eq. (2.25) for the Caesium-Lithium mass ratio $M/m \approx 22.1$ and cutoff $R_0 = 0.1k_{\mathrm{F}}^{-1}$. The steep rise of the phase shift above $\pi/2$ for $1/k_{\mathrm{F}}a = 1.85$ close to $a_+^{(1)}$ (see fig. 2.10) indicates a quasibound state.

Although all scattering details are encoded in the induced phase shifts, cf. fig. 2.9, the mediated scattering properties between the two Caesium impurities become

---

[6]using the scipy implementation of DOP853, an explicit Runge-Kutta method of order 8(5,3), see SciPy.org n.d.

more manifest when expressed as a scattering length: The induced s-wave Caesium-Caesium scattering length a_{ind} is defined by the effective range expansion as

$$k \cot \left[\delta_{l=0}^{\text{ind}}(k) \right] = -\frac{1}{a_{\text{ind}}} + \frac{r_{\text{e}}}{2} k^2 + O\left(k^4 \right) \tag{2.26}$$

thus it can be calculated from the induced scattering phase shifts in the limit $k \to 0$.
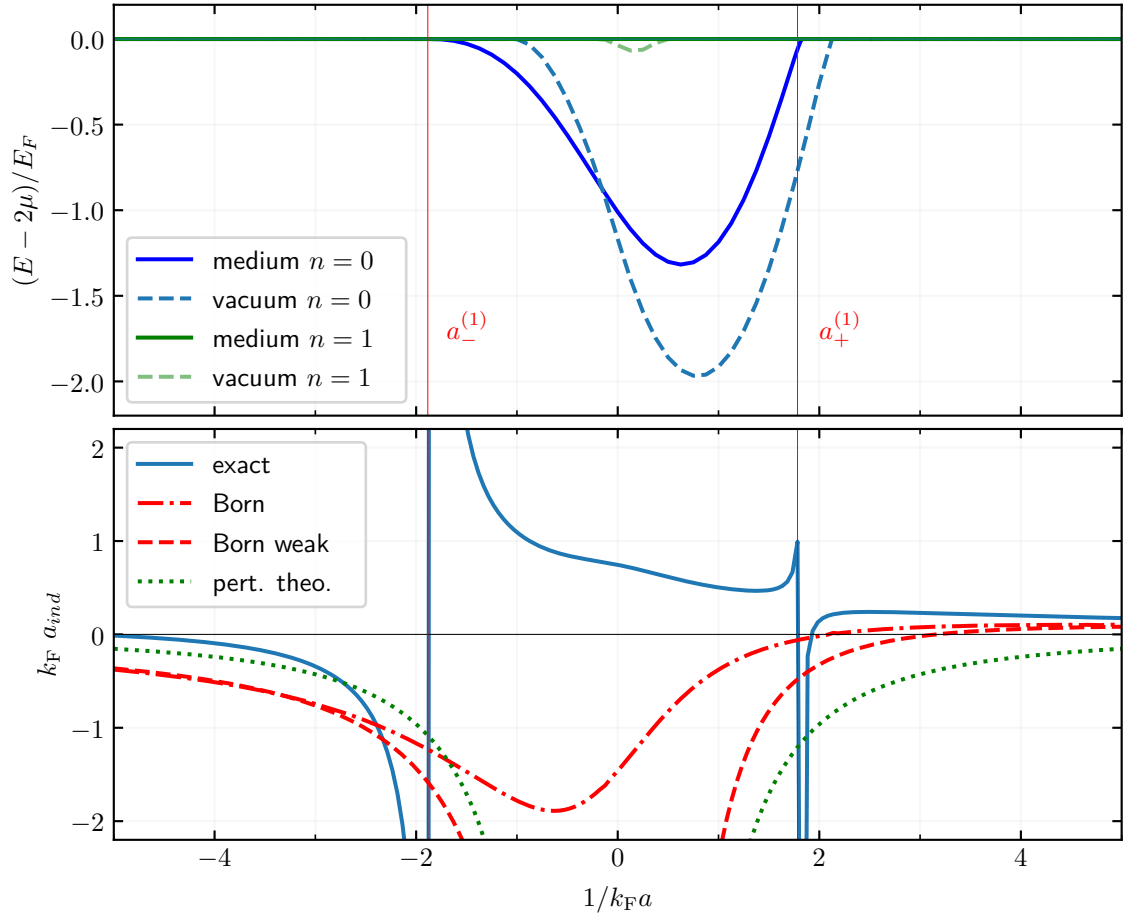
Fig. 2.10: Upper panel: Bound state spectrum relative to the scattering continuum 2μ, with ('medium') and without ('vacuum') Fermi sea. Calculations analogue to fig. 2.3 without including the Van der Waals potential. The Caesium-Caesium interaction only enters through the short range cutoff $R_0 = 0.1 k_{\text{F}}^{-1}$. In vacuum length units are $10 R_0$ and energy units $1/2m(10 R_0)^2$. Lower panel: induced s-wave impurity-impurity scattering length vs impurity-fermion interaction. Calculated by numerically integrating eq. (2.27) for Caesium-Lithium mass ratio $M/m \approx 22.1$ and cutoff $R_0 = 0.1 k_{\text{F}}^{-1}$ (blue solid line). Also shown are different approximations to a_{ind} (in red and green), for details see Enss et al. 2020.

Alternatively, the induced scattering length can be calculated integrating a similar equation as eq. (2.25) (introducing a function $\tan \delta_{l=0}^{\text{ind}}(k, R)$ and taking the limit

$k \to 0$, see Calogero and Green 1968):

$$\partial_R a_{\mathrm{ind}}(R) = MV(R)\left[R - a_{\mathrm{ind}}(R)\right]^2 \tag{2.27}$$

Here, the initial condition reads $a_{\mathrm{ind}}(R = R_0) = R_0$ and again the result is obtained in the limit $a_{\mathrm{ind}} = a_{\mathrm{ind}}(R \to \infty)$.

Note that integrating the Riccati equation for the induced scattering length, eq. (2.27), using a standard finite difference integrator as the one mentioned above is not possible due to the poles of a_{ind}, corresponding to bound states. This problem can be circumvented by a change of variables as described in Ouerdane et al. 2003: Substituting

$$a_{\mathrm{ind}}(R) = \tan\theta \qquad \text{and} \qquad R = \tan\Phi, \tag{2.28}$$

eq. (2.27) is transformed to

$$\partial_\Phi \theta(\Phi) = M\, V\left[\tan(\Phi)\right]\, \sec^4(\Phi)\, \sin^2\left[\theta(R) - \Phi\right]. \tag{2.29}$$

Eq. (2.29) can then be integrated (e.g. using the standard integrator mentioned above) starting from $\theta(\Phi_0) = \Phi_0$ where $\Phi_0 = \arctan R_0$ up to a value of Φ close to $\pi/2$.

As expected, the induced scattering length exhibits resonances at $a = a_\pm^{(1)}$, where the in-medium Efimov bound states merge with the continuum, as can be seen in fig. 2.10 (the bound state spectrum (upper panel) has been calculated using the matrix Numerov method as described above for calculations in chap. 2.2 where the results were subsequently converted to Fermi units).

It is interesting to note that these scattering resonances are not captured neither in Born approximation (red dashed and dash-dotted lines) nor in (second order) perturbation theory for weak repulsive interaction (green dotted line). This might be expected as the bound state contribution can become arbitrary large near an in-medium Efimov resonance in the exact solution. This is not captured neither by Born approximation (leading contribution to induced scattering length $\propto a$) nor by perturbation theory (leading term $\propto a^2$). For details see Enss et al. 2020.

While resonances in the induced scattering length have been expected at positions where in-medium Efimov bound states merge with the scattering continuum, to determine whether this leads to quasibound states that survive at positive energies is more subtle. To investigate this further, we again have a look at the scattering phase shift $\delta_{l=0}^{\mathrm{ind}}(k)$ as a function of k (as a measure for the scattering energy $E = k^2/2m > 0$) near the resonance position $a_+^{(1)}$ as shown in fig. 2.11 (blue, solid lines). We identify a quasibound state if the induced phase shift assumes the Breit-Wigner form

$$\cot\left[\delta_{l=0}^{\mathrm{ind}}(k)\right] = -\frac{E - E_{\mathrm{qbnd}}}{\Gamma_{\mathrm{qbnd}}/2} + \dots\, , \tag{2.30}$$

which leads to a maximum in the *s*-wave scattering cross section (red dashed lines in fig. 2.11), given by

$$\sigma_{l=0}(k) = \frac{4\pi}{k^2} \sin^2\left[\delta_{l=0}^{\text{ind}}(k)\right]. \tag{2.31}$$

The resonance position E_{qbnd} and -width Γ_{qbnd} can be extracted from the position of the zero crossing and the slope in its vicinity of $-\cot\left[\delta_{l=0}^{\text{ind}}(k)\right]$ (dotted blue line).
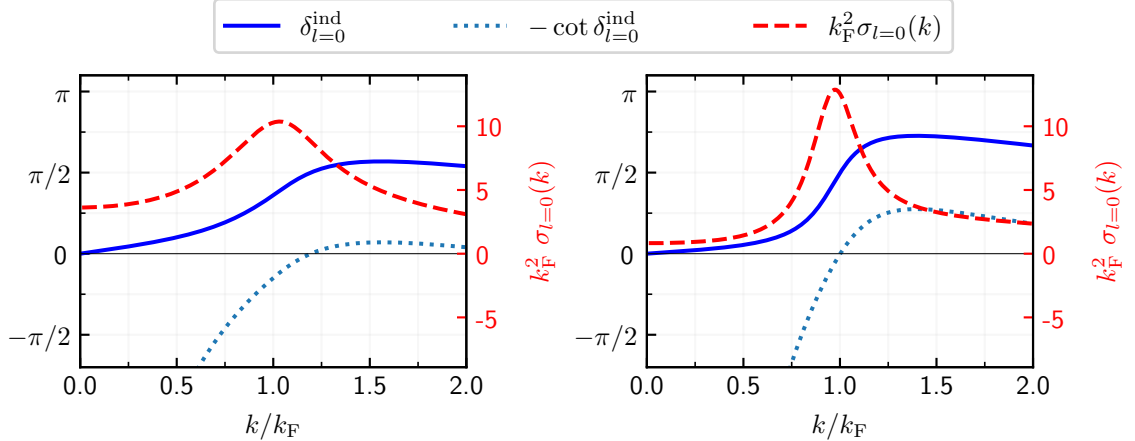

Fig. 2.11: Left panel: Induced scattering length (blue solid) for $k_{\text{F}}a = 0.536$ near the resonance position $k_{\text{F}}a_+^{(1)} = 0.542$ for the Caesium-Lithium mass ratio $M/m \approx 22.1$. Also shown are its cotangent $-\cot\left[\delta_{l=0}^{\text{ind}}(k)\right]$ (dotted blue) and the resulting scattering cross section (eq. (2.31), red dashed line shown on a separate scale). Right panel: Same as left panel, now for twice the Caesium-Lithium mass ratio $M/m = 2(M/m)_{\text{CsLi}} \approx 44.2$. In this case $k_{\text{F}}a = 0.3596$ close to the resonance position $k_{\text{F}}a_+^{(1)} = 0.360$.

From fig. 2.11 we can conclude that there is enhanced scattering near the in-medium Efimov resonance $a_+^{(1)}$ for the Lithium-Caesium system (left panel) but the resonance is so broad ($\Gamma_{\text{qbnd}} \gtrsim E_{\text{qbnd}}$) that one would not call this a well-defined quasibound state. For larger mass ratios $M/m \gtrsim 40$ however, the resonance is sharper, e.g. for $M/m \approx 44.2$ (right panel) we find $\Gamma_{\text{qbnd}}/E_{\text{F}} \approx 0.69 < E_{\text{qbnd}}/E_{\text{F}} = 1.02$ which can be identified as a well-developed quasibound state. This can be understood as increasing the mass ratio also increases the effective height of the potential in the Schrödinger equation (2.23), leading to a higher repulsive barrier and thus longer lived quasibound states.

In the preceding part we investigated how the presence of a Fermi sea alters both the bound state spectrum and the scattering properties of two heavy bosons mediated by one (or many) fermion(s). The transition of the bound state spectrum of two impurities immersed in a Fermi sea to the well-known Efimov effect has been investigated in figures 2.3 and 2.4, where we also included the Caesium-Caesium Van der Waals interactions. These lead to deviations from the 'pure' Efimov spectrum,

which can explicitly be seen in fig. 2.6. These deviations can be understood as coming from a change in the effective Caesium-Caesium potential that significantly deviates from the $1/R^2$ form at small distances, see fig. 2.7. Increasing the fermion density has a similar effect but in this case the potential is altered at larger distances where the new length scale introduced by the Fermi sea - the Fermi momentum k_F - not only cuts off the infinite progression of Efimov bound states, but also leads to an altered scaling law (fig. 2.8).

Regarding the scattering properties of two Caesium atoms immersed in a Fermi sea, we find that indeed the fermionic background imprints its signature (see fig. 2.10) that manifests itself as enhanced scattering at the resonance positions where the in-medium Efimov bound states merge with the scattering continuum. For large mass ratios and positive interspecies scattering length we also find that the in-medium Efimov states 'live on' as quasibound states at positive energies which we interpret as two impurities caught behind the barrier created by the Fermi sea, cf. fig. 2.11.

Most of the theoretical results obtained so far can be experimentally verified in an ultracold mixture of Caesium impurities immersed in a Lithium Fermi sea, further discussed in chap. 4. This is why, instead of refining the theoretical description, we will focus on working towards an experimental realisation of the polaron scenario in the remainder of this work.

3 Upgrading a Caesium Bose-Einstein Condensate

After having discussed some theoretical aspects of the Fermi polaron in the first part of this thesis, I now turn to the description of an experiment aiming at investigating a closely related - or complementary - problem: the Bose polaron. Here the idea is to immerse a few impurities (in our case ^{6}Li atoms) into a bath consisting of a Bose-Einstein condensate (in this experiment of ^{133}Cs atoms). Cooling a mixture of two very different quantum gases to sufficiently low temperatures and at the same time high densities to reach a Bose-Einstein condensate (BEC) is a very challenging task. The large differences in mass, polarisability and magnetic moment require a sophisticated scheme of sample preparation: Starting from a custom-made double-species Zeeman slower, two magneto-optical traps (MOT) are loaded sequentially from where, after further cooling mechanisms have been applied, each species is loaded into its own optical dipole trap and evaporatively cooled before they are finally combined. Details on the experimental apparatus and the loading scheme can be found e.g. in Pires 2014; Lippi et al. 2021.

In the existing Mixtures experiment the limiting factor that prevented the observation of Bose polarons so far is the Caesium BEC which can only be produced with such a low number of atoms that it is too fragile to be mixed with Lithium. In the following, we will therefore investigate several crucial steps during the creation of a Caesium BEC.

First, the loading of Caesium in the so-called 'reservoir trap' (RT), a large-volume optical dipole trap, is investigated in sec. 3.1. We will focus on the fast switching of magnetic fields which facilitates the efficient loading in the levitated RT, i.e. when the gravitational potential is cancelled by a magnetic gradient field.

Next, we are going to have a closer look at the adiabatic phase space density enhancement (also referred to as 'dimple trick') in sec. 3.2, which allows a local increase of phase space density by means of a second, smaller dipole trap, the so-called 'dimple trap' (DT). We will model this process theoretically, compare our model with the experiment and use it to suggest improvements beyond the current experimental setup.

Furthermore, we will theoretically and experimentally investigate the process of forced evaporative cooling in sec. 3.3, which is used after the dimple trick to reach the critical phase space density such that the Caesium cloud undergoes Bose-Einstein condensation.

Lastly, different limits on the number of Lithium impurities in the final mixture are considered in appendix A.1, stemming from our absorption imaging system as well as the onset of quantum degeneracy (preferably, Lithium should be non-degenerate

in order to investigate the usual Bose polaron scenario while it is held in tightly focussed 'micro trap', cf. Klaus 2019).

## 3.1 Upgraded loading of reservoir dipole trap

After the Caesium MOT is loaded and a sub-Doppler cooling scheme is applied, the cloud is further cooled to the lowest hyperfine state $|F = 3, m_F = 3\rangle$ using degenerate Raman sideband cooling (dRSC). From here, the atoms have to be transferred to the reservoir trap (RT), a large-volume crossed beam dipole trap (retro-reflected 1064 nm, 55 W beam at a crossing angle of 90° with a waist of $\sim 320\,\mu$m). The Caesium atoms are loaded into the RT either with or without a magnetic gradient field. The gradient field is used to 'levitate' Caesium, i.e. it is tuned to counteract the gravitational pull which would tilt the trapping potential along the so-defined z-direction, cf. fig. 3.1. To understand the importance of the decision whether to use magnetic levitation or load the RT only optically, we will shortly have a look at the consequences of both scenarios in the following.

Having in mind the mixing with Lithium, one has to consider that a magnetic gradient field tuned to levitate Caesium will largely over-levitate Lithium due to their different magnetic moments. This will lead to complications in the mixing which can be overcome by either getting rid of the gradient before applying the dimple trick or by using at least three different optical traps (see also the discussion at the very end of this chapter). But even when considering only Caesium, the use of a shallow levitated RT puts demanding constraints on the minimal switching times of the magnetic fields: Both gradient and offset fields have to be switched on directly after the dRSC, together with the RT. While the offset field only has to reach a quite low value (< 50 G) to mitigate the anti-trapping in the x- and y-direction due to the quadrupole gradient field, the gradient field itself has to be switched on fast compared to the time it takes atoms to leave the trapping region of the RT: The atoms that leave the trapping region during the switch-on time of the magnetic fields (due to gravity or the expansion of the cloud) will not be loaded into the RT, leading to a reduced transfer efficiency, see also sec. 3.1.1.

In the presence of these problems, it is instructive to have a look at an alternative sequence where one tries to obtain a BEC without the use of a levitation gradient field. There are two main disadvantages to this approach that will be shortly discussed here.

First, without levitation, the mode matching between the Caesium cloud after dRSC and the RT is far from optimal: From measurements of the number of atoms, the size and temperature of the Caesium cloud after dRSC, we conclude that although the spatial extension of the cloud should well fit into the RT volume, the temperature and hence momentum of the cloud is very different from the corresponding equilibrium values in the RT. E.g. for a MOT load time of 300 ms which in the current setup is the maximal load time compatible with Lithium stored in

Fig. 3.1: Comparison of exemplary trapping potentials (with arbitrary offsets) for Caesium in the reservoir trap with (upper panel) and without (lower panel) levitation magnetic gradient field along x- and y- (blue solid) and z-axis (orange dashed line). The laser power is adjusted such that the potential in the least trapping direction is $U/k_\mathrm{B} \approx 10\,\mu\mathrm{K}$. In the non-levitated case this leads to trap depths in the stronger trapping directions of $U/k_\mathrm{B} \approx 60\,\mu\mathrm{K}$.
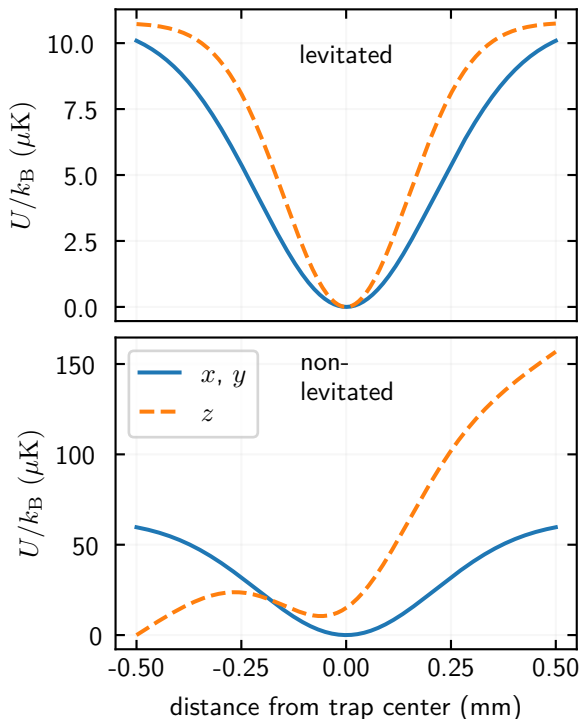
the DT[1], the dRSC cloud has a $1/e$-extension[2] of about $\sim 220\,\mu\mathrm{m}$ (compared to a RT beam waist of $\sim 320\,\mu\mathrm{m}$, in principle allowing MOT load times up to $\sim 1\,\mathrm{s}$). The cloud's mean temperature at $300\,\mathrm{ms}$ MOT load time is $T \approx 1\,\mu\mathrm{K}$ which should be matched by a trap depth U of roughly a factor 10 higher: For harmonic traps in thermal equilibrium (demanding very low plain evaporation) $U/k_\mathrm{B}T \approx 10$, cf. Olson et al. 2013 and discussion in sec. 3.3.

This, however, can not be fulfilled in all spatial directions without levitation: Without the additional magnetic gradient field the optical power needed to provide a sufficiently deep trapping potential along the axis of gravity at the same time leads to a potential that is much too deep in the perpendicular directions ($U_{x,y}/k_\mathrm{B} \approx 80\,\mu\mathrm{K}$), see fig 3.1, leading to considerable heating of the sample during transfer.

Second, the gradient field also acts as a filter for the different hyperfine sub-levels: Because of their different magnetic moments, specific sub-levels are levitated at specific gradient fields, while all other sub-levels experience considerably different gradients leading to them not being trapped any more. This becomes important when considering that dRSC does not fully spin-polarize the sample (as it theoretically should) but only reaches a polarization in the $|F = 3, m_F = 3\rangle$ state up to $85\,\%$. The remaining atoms are mostly in the $|F = 3, m_F = 2\rangle$ state, which - by

---

[1]In the experimental mixing sequence Lithium is loaded first and stored in the 'dimple trap', before Caesium is loaded at an off-centred position. The final separation of the two clouds directly limits the size and load time of the Caesium MOT.

[2]we do not strictly expect a Gaussian cloud shape but the fit provides a reliable estimate of the cloud size

Fig. 3.2: Cut along reservoir trap potentials for Caesium along an axis perpendicular to gravity. The magnetic gradient field, tuned such that Caesium is levitated (gravitational potential cancelled in z-direction), leads to anti-trapping in x- and y-direction, depending on the value of the offset field B_0 (increasing from dark to light).
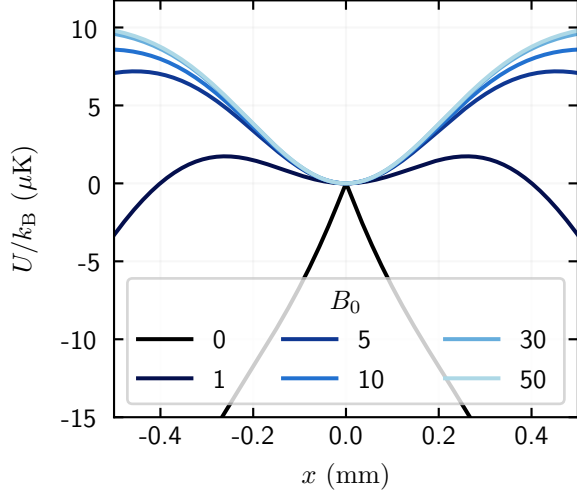
undergoing spin-changing-collisions - can lead to significant two-body losses. Even with purifying the sample by resonantly heating the $|F = 3, m_F = 2\rangle$ atoms out of the trap, we could not increase the Caesium lifetime in the non-levitated RT.

Because of the much better mode matching of the Caesium cloud after dRSC and RT we will from now on focus on the creation of a BEC using a magnetic gradient field to levitate Caesium when loading the RT.

3.1.1 Dipole trap loading with magnetic levitation

For an efficient loading of the RT, fast switching of the magnetic fields is essential: During the time it takes for the gradient field to reach a minimal value, atoms from the expanding cloud will not be trapped, leading to an inefficient transfer. At the same time, also the magnetic offset field has to be switched on to mitigate the anti-trapping effect of the gradient field, see fig. 3.2.

The gradient field is produced by two coils in anti-Helmholtz configuration ('curvature coils') which generate a quadrupole field that, in the vicinity of the centre between the two coils, is well approximated by a linear gradient field along the symmetry axis of the coils which in the experiment is parallel to the gravitational acceleration (by definition parallel to the z-axis). Without an additional magnetic offset field, this quadrupole field leads to an anti-trapping potential in the perpendicular x- and y-directions, see fig. 3.2. The magnetic offset field is generated by a pair of coils in Helmholtz-like configuration ('Feshbach coils'), generating a homogeneous field in the vicinity of the centre between the coils where the atoms are located. Each pair of coils is powered by a separate power supply, in steady state supplying a constant and controlled current. For the gradient field the current control of the power supply is used directly, while the offset field is externally stabilized using a current transducer as a feedback for a PID controller. The target value of the PID controller as well as the limiting current of the gradient field power supply can be controlled via the experimental control (FPGA based sequencers). Also the

maximal voltage of the gradient field (CURV CV) and the maximal current of the offset field (FB CC) - the PID being connected to the maximal voltage (FB CV) - can be controlled via the experimental control.

When switching times are not crucial, magnetic fields are normally switched by setting the current control (CC) to the new desired value and leaving the limiting voltage (CV) sufficiently high[3].

Let us consider a positive (from lower to higher value) and small jump, i.e. a jump that does not exhaust the power supply's capacities. The (internal our external) controller will regulate the power supply's voltage slowly enough, so that the current does not overshoot the target value. Considerably faster switching times can be achieved when the full power of the power supply is used: Here the idea is that at the time when the field is to be switched, both control inputs of the power supply (via the external PID, where applicable) are set to their maximum and when the current through the coil reaches the desired level, they are set to the values needed to produce the desired steady state. In practice the process is slightly more involved as the (internal or external) controllers show oscillatory behaviour when the target values are switched in this fast way, which makes it necessary to fine-tune the exact switching times, as well as the level of the free control input (CURV CV or FB CC) depending on the size of the jump. This tedious process could be avoided by using a digital, programmable PID controller which could be disabled during the fast switching process and is subsequently set to the new steady state. Bypassing the analogue PID controller that is currently built into the experiment does not help as e.g. the integral value of the controller would have to be reset externally to avoid transient oscillations when turning the controller back on. An exemplary switching sequence used during the transfer of the Caesium cloud after dRSC to the reservoir trap is shown in fig. 3.3.

With the possibility of switching the magnetic fields in $\sim 1\,\mathrm{ms}$, one can attempt to implement the following compression and cooling scheme: The Caesium atoms, after being cooled using dRSC in free space, are transferred to the RT as described above. Then, when the dRSC lattice is switched off, after a quarter of an oscillation period defined by the harmonic approximation of the RT potential, the atoms should have transferred most of their potential energy to kinetic energy by 'rolling down' the potential towards the centre of the trap. At this point, one could turn on the Raman lattice again, and remove the atoms' kinetic energy by another cycle of dRSC. This would require to get rid of all magnetic fields within a period of a few milliseconds, which turns out not to be possible within our current experimental setup:

When either pair of coils is to be switched off, the coils are disconnected from their power supply by opening a set of MOSFETs and the energy stored in the coils is dissipated through a set of varistors parallel to the coils, for details and characterization see Freund 2019. This setup allows to switch off the current in the Feshbach coils in less than $700\,\mathrm{\mu s}$. However, the magnetic field is present much

---

[3]This would be the case for the gradient fields. For the offset field, one would switch the PID target value and correspondingly leave the CC on a sufficiently high level.
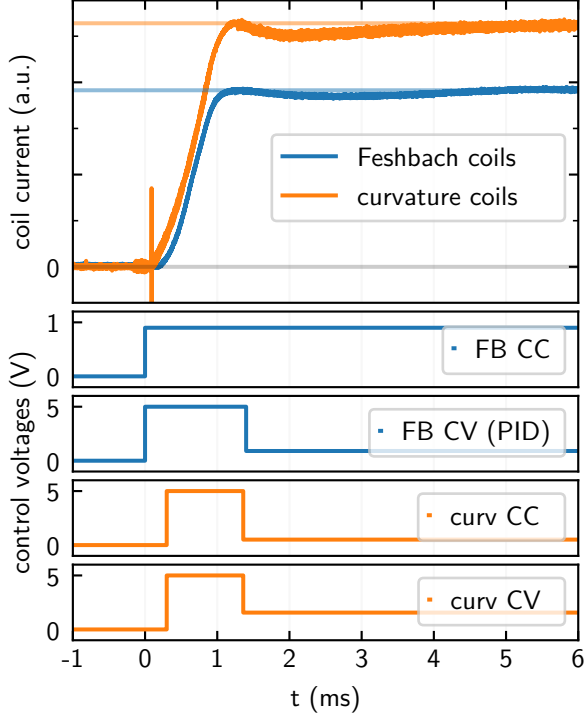
28

Fig. 3.3: Fast switching used during loading of the reservoir trap after dRSC. Upper panel: time dependence of the coil currents (measured using two current transducers), remaining lower panels: time dependence of the control signals. Gradient field ('curvature coils', curv) switched to final value of $31\,\mathrm{G\,cm^{-1}}$ and offset field ('Feshbach coils', FB) to $\sim 200\,\mathrm{G}$ (both marked as horizontal lines). Achieved switching time of $\sim 1\,\mathrm{ms}$ with minimal oscillations.

longer than this timespan, supposedly due to Eddie currents in the conducting parts of the vacuum chamber: In fig. 3.4 we measured the magnetic field next to the vacuum chamber with a magneto-resistive sensor (Honeywell HMC2003, all axes recorded on a digital oscilloscope) and directly at the atoms' position using Lithium spectroscopy[4] and compare the results to the coil currents.

Without major changes to the experiment (at least adding coils that actively counteract the magnetic field induced by the Eddie currents, in the worst case replacing the science chamber with a glass cell) one could attempt to hold the atoms in the Raman lattice while the magnetic fields decay. But it turns out that holding the Caesium atoms in the Raman lattice for $\sim 15\,\mathrm{ms}$ (the time it takes for the offset field to drop to a level where dRSC works) leads to considerable heating due to scattering with the near-resonant Raman lattice light, effectively preventing the use of multiple Raman cooling cycles.

With the fast switching of the magnetic fields as described above (only one Raman cooling cycle), we are able to load 2.5×10^6 Caesium atoms at a temperature of $1.2\,\mathrm{\mu K}$ into the RT. These values refer to a Caesium MOT load time of $300\,\mathrm{ms}$

---

[4]For magnetic fields $B \gtrsim 150\,\mathrm{G}$ we can use the offset-locked D_2 Lithium 'high-field imaging' laser (for principle and setup, see e.g. Heck 2012) to measure the time when the atoms are subject to a specific magnetic field: We set the laser frequency to a value corresponding to a certain magnetic field and record the time after (before) the switch on (off) when it is resonant with the transition. The first (last) point at zero magnetic field is recorded in a similar manner using Lithium 'low field' imaging, see Pires 2014. Due to technical limitations in the current setup we are not able to measure finite magnetic fields below $\sim 150\,\mathrm{G}$ with these methods.
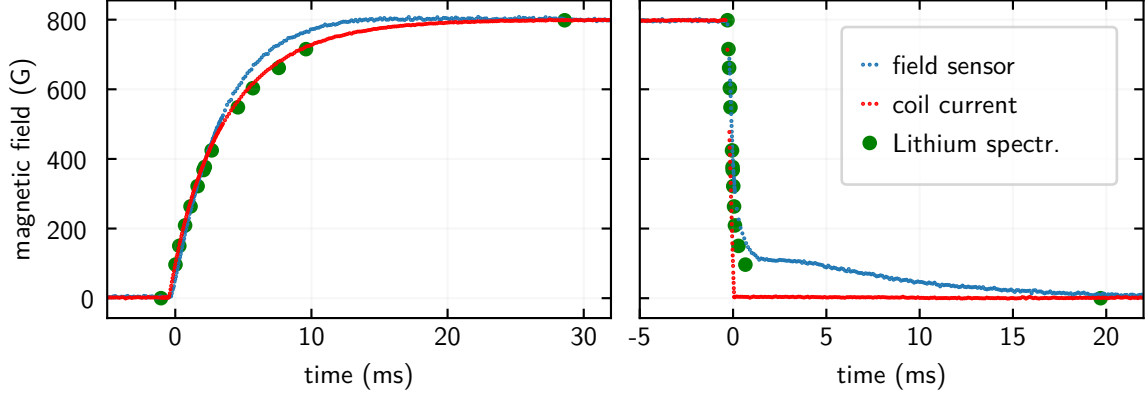
Fig. 3.4: Exemplary offset magnetic field jump from $0\,\mathrm{G}$ to $\sim 800\,\mathrm{G}$ (left panel) and back to $0\,\mathrm{G}$ (right panel) as measured by a magneto-resistive HMC2003 sensor (blue), current transducer (red) and Lithium spectroscopy (green dots). The deviation during switch-on might be explained by the different placement of the HMC2003 (outside the vacuum chamber), during switch-off it is evident that the magnetic field decays much slower than the coil current would indicate, which we attribute to Eddie currents. Calibration of the different measurements performed in steady-state.

where we end up with $\sim 4.4 \times 10^6$ atoms after dRSC, resulting in a transfer efficiency $> 55\,\%$. For longer Caesium MOT load times the absolute number of atoms loaded into the RT can be considerably improved (e.g. for $2\,\mathrm{s}$ MOT load time we can load $\sim 8 \times 10^6$ atoms) which is mostly due to the increased atom density near the centre of the Raman cloud, not the larger atom number in the cloud after dRSC (i.e. the transfer efficiency drops for larger Raman clouds, as the RT trapping volume is limited by the beam waists).

Concluding, the fast switching described here enables us to efficiently load a shallow (i.e. mode-matched) reservoir trap which results in much better initial conditions for adiabatically enhancing the phase space density and subsequent evaporation which ultimately also improves the final BEC, see also chap. 4.

3.1.2 Fast Feshbach switching

The intended polaron experiments are only possible because of a broad Lithium-Caesium Feshbach resonance close to $890\,\mathrm{G}$ in combination with a Caesium three-body loss minimum at $\sim 893\,\mathrm{G}$. This means that at some point after the dRSC (which only works without external magnetic fields), we have to jump to high magnetic offset fields. When changing the magnetic field across a large range, one will inevitably cross Feshbach resonances that will dramatically enhance Caesium three-body losses. Bearing in mind that the three-body losses are unitarity limited at a given temperature, c.f. fig. 3.12, one wants to jump to high magnetic fields as early

in the sequence as possible (after dRSC, which requires almost zero offset fields), before cooling the cloud to low temperatures.

Later, during plain or forced evaporation, one ideally wants to have high two-body scattering rates (needed for fast re-thermalization) and low three-body scattering rates (only leading to trap losses). While this interplay will be investigated more carefully in sec. 3.3, it gives the intuition needed to find the best way of getting to the desired high magnetic fields: We first jump to an offset field of $\sim 600\,\mathrm{G}$ as fast as possible (cf. sec. 3.1.1) and then ramp up the magnetic field during $1\,\mathrm{s}$ to a final level of $943\,\mathrm{G}$, corresponding to a relatively high Caesium-Caesium scattering length of $\sim 840\,a_0$ facilitating fast thermalization. During this ramp, atoms are lost from the RT but the temperature decreases, i.e. the magnetic field ramp is used to cool the atoms by forced evaporation. This combination of magnetic field jump and evaporation ramp has been experimentally optimized to give the best starting conditions in the reservoir trap for enhancing the phase space density by adiabatically changing the trapping potential which will be investigated in the following section.

3.2 Upgraded adiabatic phase space density enhancement

To reach Bose-Einstein condensation, the phase space density (PSD) $\Gamma = n\lambda_{\mathrm{dB}}^3$ has to be increased beyond a critical value of the order of one (for an ideal Bose gas $\Gamma > \zeta(3/2)$). This can be achieved by any combination of increasing the atom density n or decreasing the temperature T, thus increasing the thermal de Broglie wavelength $\lambda_{\mathrm{dB}} \equiv h/\sqrt{2\pi m k_B T}$. During most of the cooling process, the PSD is increased by evaporation (cf. sec. 3.3), i.e. by letting the hottest, most energetic atoms 'escape' from the trap. In order to reach a BEC with high atom numbers one would ideally try to increase the PSD in a reversible, i.e. adiabatic way. Unfortunately, theoretical mechanics forbids a global increase of PSD under adiabatic transformations, but nevertheless, a *local* PSD increase using only adiabatic trap deformations is possible. The idea behind this is that by adding an attractive potential locally (the 'dimple') the local density is increased but as the dimple is still in thermal contact with the larger, unaltered part of the potential (the 'reservoir'), the temperature increase is reduced compared to a global potential deformation. This idea also goes under the name of 'dimple trick' and was first discussed in Pinkse et al. 1997, while in Stamper-Kurn et al. 1998 the reversible formation of a BEC was first demonstrated using this technique.

In the current setup of our Lithium-Caesium mixture experiment, Lithium is already in the smaller dimple trap compared to the larger Caesium reservoir trap, such that while mixing the two species by overlapping the traps, the change in potential can be used as a dimple trick for Caesium (hence the names of the traps).

In this chapter, I want to briefly discuss the maximal increase in PSD that is

theoretically achievable and the parameters it depends on, first following Stamper-Kurn et al. 1998 for a qualitative understanding, then in a slightly more involved model that uses experimental parameters in sec. 3.2.1. After checking that the model adequately reproduces our current experimental measurements, we will be able to use the model to explore parameter regimes where the phase space density enhancement is even larger, also taking into account the constraints imposed by Lithium in sec. 3.2.2.

3.2.1 Theoretical model

Closely following Stamper-Kurn et al. 1998, I will introduce the concepts needed to model the change in temperature, atom densities and thus also phase space density during the dimple trick. As in the cited article, let us consider the following situation: The atoms are confined to a region of space that is made up of two sub volumes V_1 and V_2. Initially, the atoms can move freely between these two volumes and do not experience any different potentials. Then, an additional, attractive potential U is added adiabatically, only affecting the atoms in V_2. Thus, the only free parameters in this model are the final potential U in V_2 and the ratio V_1/V_2. As we assume that the number of atoms is conserved, we work in the canonical ensemble and should be able to derive all quantities of interest from the canonical partition function and its derivatives. The single particle partition function in terms of inverse temperature $\beta \equiv 1/k_B T$ is given by

$$z = \int d^3x \int d^3p \ \exp\left[-\beta\left(\frac{p^2}{2m} + V(x)\right)\right] = \lambda_{\text{dB}}^{-3}\left(V_1 + V_2 e^{\beta U}\right) \ , \tag{3.1}$$

where we again use the thermal de Broglie wavelength $\lambda_{\text{dB}} \equiv h/\sqrt{2\pi m k_B T}$. Here, the potential $V(x)$ equals $-U$ (where $U > 0$) if $x \in V_2$ and is zero elsewhere. From the single particle partition function z, under the assumption of having N identical particles, we can derive the free energy $F = -N k_B T \log z$ and from there the entropy

$$S = -\partial_T F = k_B N \left(-\frac{\beta\, U}{e^{-\beta U}\left(V_1/V_2\right) + 1} + \log\left(\frac{V_1 + e^{\beta U} V_2}{\lambda^3}\right) + \frac{3}{2}\right) \quad . \tag{3.2}$$

Demanding that the lowering of the additional potential is adiabatic, i.e. the entropy is conserved, we can derive an expression for the temperature change as a function of the final potential U and the ratio of the volumes:

$$0 \stackrel{!}{=} \Delta S \equiv S(T, U) - S(T = T_0, U = 0)$$
$$\Rightarrow \log\left(\frac{T_0}{T}\right)^{3/2} = -\frac{TU/k_B}{\left(V_1/V_2\right) e^{-\beta U} + 1} - \log\left(\frac{V_1 + V_2}{V_2 e^{\beta U} + V_1}\right) \quad . \tag{3.3}$$

From the single particle partition function we can furthermore calculate the mean energy per particle $\langle E \rangle / N = -\partial_\beta z$. Assuming that the mean kinetic energy per
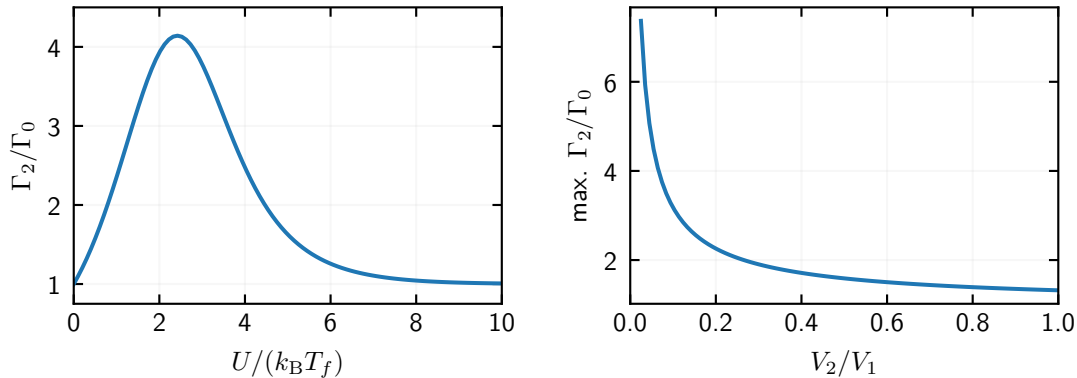
Fig. 3.5: Left panel: Phase space density gain for $V_2/V_1 = 1/16$ as a function of the potential in V_2 as predicted by the model of Stamper-Kurn et al. 1998. Right panel: Maximally reachable phase space density gain for different ratios of V_2/V_1.

particle is $3k_\mathrm{B}T/2$, we can derive an expression for the mean potential energy per particle as a function of U and from there the fraction of atoms in the volume V_2 and the corresponding atom density fraction:

$$\frac{N_2}{N} = 1 - \frac{1}{(V_2/V_1)e^{\beta U} + 1}; \qquad \frac{n_2}{n} \equiv \frac{N_2}{V_2}\frac{V_1 + V_2}{N} = \frac{e^{\beta U}(V_1 + V_2)}{V_2 e^{\beta U} + V_1} \ . \tag{3.4}$$

Now we have all that we need to calculate the increase in PSD Γ_2 in V_2 compared to the PSD before the lowering of the additional potential Γ_0 (eq.1 in Stamper-Kurn et al. 1998)

$$\log\left(\frac{\Gamma_2}{\Gamma_0}\right) = \log\left(\frac{n_2}{n_0}\right) + \log\left(\frac{T_0}{T}\right)^{3/2} = \frac{U/(k_\mathrm{B}T)}{1 + (V_2/V_1)e^{U/(k_\mathrm{B}T)}} \quad . \tag{3.5}$$

Estimating the volumes of reservoir and dimple traps from the volumes enclosed by the crossing laser beams, we estimate $V_2/V_1 \approx 1/16$ (cf. fig. 3.5). For this ratio, eq. (3.5) predicts a maximally reachable PSD gain of 4 which is a fairly good estimate as we shall see below in sec. 3.2.2.

Note, that in eq. (3.5) the potential depth U in V_2 is measured in units of the *final* temperature T. To calculate the final temperature as a function of the initial temperature and final potential depth U, we can (numerically) solve eq. (3.3) or equivalently integrate the differential equation resulting from the differential form of adiabaticity, $TdS = 0$ (where the entropy S depends on T and U).

Although the qualitative dependence of the dimple trick's outcome is well described by this simple model, it does not adequately describe our setup in terms of experimentally relevant parameters (reservoir trap depth, density distributions, ...). This is why in the next section we want to further refine this model and employ a description that is closer to our experimental setup.
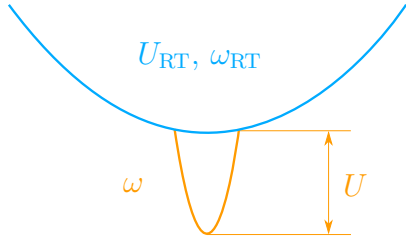
Fig. 3.6: Approximation of reservoir and dimple traps as two harmonic potentials, each parametrized by trap depth and trap frequency.

Harmonic model. Although the dimple trick has been extensively modelled using e.g. Monte Carlo simulations, cf. Ma et al. 2004, here we want to gain some insights using a rather simple harmonic approximation of our potential: We approximate reservoir and dimple traps by two spherically symmetric harmonic potentials, each parametrized by a trap depth U and a mean harmonic trapping frequency ω, see fig 3.6. Without subscript, these parameters refer to the dimple trap, the subscript 'RT' marks parameters of the reservoir trap. In this approximation, each potential is given by

$$V_i(r) = \frac{m_{\mathrm{Cs}}}{2k_{\mathrm{B}}}\omega_i^2 r^2 - U_i \ , \qquad r \leq r_{\mathrm{max},i} \equiv \frac{\sqrt{2k_{\mathrm{B}}U_i/m_{\mathrm{Cs}}}}{\omega_i} \ . \tag{3.6}$$

Note, that the mean trapping frequencies scale as $\omega_i \propto \sqrt{U_i}$, i.e. their dependence is fixed by $\omega_i = \omega_{0,i}$ at $U_i = U_{0,i}$ such that $\omega_i(U_i) = \omega_{0,i}\sqrt{U_i/U_{0,i}}$. The combined potential is then simply given by $V(r) = V_{\mathrm{RT}}(r) + V_{\mathrm{dimple}}(r)$ and is parametrized by U_{RT}, ω_{RT}, U and ω.

From here, we follow the same steps as described above: From the potential we calculate the single particle partition function, the free energy and the entropy. By imposing adiabaticity, we can calculate the change in temperature during the dimple trick. From there, we can calculate the thermal density distribution

$$n_{th}(r) = \lambda_{\mathrm{dB}}^{-3} \, \mathrm{Li}_{3/2}\left(e^{\beta(\mu - V(r))}\right) \tag{3.7}$$

where we fix the chemical potential μ by assuming conservation of total particle number N and imposing

$$N \stackrel{!}{=} \int d^3x \ n_{th} \quad . \tag{3.8}$$

In the equations above, Li denotes the Polylogarithm, e.g. defined by its series representation, cf. Wolfgang Ketterle and Zwierlein 2008

$$\mathrm{Li}_s(z) = \sum_{j=1}^{\infty} \frac{z^j}{j^s}, \quad |z| \leq 1. \tag{3.9}$$

The results of the calculations for the harmonic model described above for the current experimental parameters can be seen in fig. 3.7. For a discussion of the current
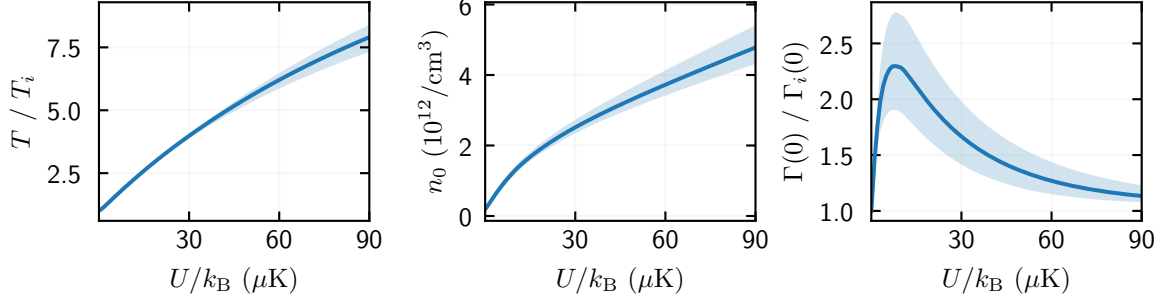
Fig. 3.7: Theoretical simulation of the dimple trick for typical experimental parameters. From left to right: Temperature increase (compared to temperature T_0 in the RT before the dimple trick), peak atom density n_0 (measured in the trap centre) and peak PSD increase (peak PSD in the combined traps $\Gamma(0)$ compared to the peak PSD in the RT before the dimple trick $\Gamma_{\mathrm{RT}}(0)$). Simulation for $U_{\mathrm{RT},0}/k_{\mathrm{B}} = 9.1\,\mu\mathrm{K}$, $\omega_{\mathrm{RT}}(U_{\mathrm{RT},0}) = 121\,\mathrm{s}^{-1}$, $\omega_0 = 448\,\mathrm{s}^{-1}$ at $U_0/k_{\mathrm{B}} = 18.4\,\mu\mathrm{K}$, $N = 9.7 \times 10^5$ and $T_0 = 1.1\,\mu\mathrm{K}$. The shaded areas mark the tolerances due to uncertainties in the experimental beam waist determination (influencing $\omega(U)$ and $\omega_{\mathrm{RT}}(U_{\mathrm{RT},0})$, see sec. 3.2.2).

experimental parameters and their uncertainties, see sec. 3.2.2. The overall shape of the phase space density gain (right panel of fig. 3.7) matches our expectations and looks quite similar to the one obtained with the two-box model, cf. fig. 3.5, except now we are in a position that we can quantitatively compare the absolute numbers to the experiment, which will be the next section's topic.

3.2.2 Experimental implementation and improvements

Now that we gained a theoretical understanding of the working of the dimple trick, we would like to experimentally verify our model in order to confidently use it to simulate the effects of modifications to our current experimental setup.

To compare to theory, we first need to know all relevant parameters needed to describe the dimple trick: the trapping frequencies of reservoir and dimple traps (the latter as a function of the dimple trap laser power) and both trap depths, for the dimple again as a function of the laser power. Both trapping frequencies and trap depths can be inferred when the waist and power of the trap beams are known. For that, first a laser power calibration is performed (linking values in the experimental control to the laser powers ideally at the atoms' position, in this case measured before the vacuum chamber). Then, trapping frequencies are measured (for the RT using direct observation of the centre of mass motion of a Caesium cloud, for the dimple trap using parametric heating and associated atom losses in a Lithium sample) at different laser powers and the beam waists are obtained from a least-squares fit (Grimm et al. 2000). We obtain $w_{0,\mathrm{RT}} = (320 \pm 15)\,\mu\mathrm{m}$ for the RT and $w_{0,\mathrm{DT}} = (62 \pm 1)\,\mu\mathrm{m}$ for the dimple trap. From there, we calculate $\omega_{0,\mathrm{RT}} = 121\,\mathrm{s}^{-1}$

at $U_{0,\mathrm{RT}}/k_\mathrm{B} = 9.1\,\mu\mathrm{K}$ initially in the RT and $\omega_0 = 448\,\mathrm{s}^{-1}$ at $U_0/k_\mathrm{B} = 18.4\,\mu\mathrm{K}$, determining $\omega(U)$ in the dimple trap. The uncertainties in the beam waists translate to uncertainties in $\omega(U)$ and $\omega_{\mathrm{RT}}(U_{\mathrm{RT}})$ used in the theory calculations (marked as shaded areas, see e.g. fig. 3.7) and all derived experimental quantities (marked as upper and lower bounds, see e.g. fig. 3.8).

Apart from the above mentioned parameters, we need to measure the initial atom number and temperature in the reservoir trap as well as the final density distribution (or the number of atoms in the dimple trap only) together with the final temperature in the combined traps. While measuring the initial atom number as well as initial and final temperatures is standard procedure (atom number extracted from two-dimensional Gaussian fit to optical depths (OD) after absorption imaging; temperature extracted from fit to cloud size for different time of flight expansions and subsequent fit), measuring the final density distribution is more involved: As the densities - and hence also the OD - get very high in the dimple trap, in-situ[5] imaging would not yield precise results. Therefore we resort to imaging only the atoms inside the dimple trap and infer their density distribution using the known trapping potential. To image only the atoms in the dimple trap (i.e. not those that are still in the reservoir trap), we apply the following scheme: After the dimple trap has been adiabatically[6] ramped up during a time of $t = 150\,\mathrm{ms}$ and the atoms thermalized, we go to a magnetic field where Caesium is non-interacting, turn off the reservoir trap and wait a variable time t_{hold} before imaging the cloud. For short t_{hold} we still record the signal of the atoms that were in the reservoir trap before, i.e. to extract the desired number of atoms in the dimple trap we can average over the signal for sufficiently long t_{hold} where the contribution to the OD from the reservoir trap atoms is negligible.

The results of these measurements are presented in fig. 3.8. Regarding the number of transferred atoms (right panel), we observe that during the dimple trick only $\sim 80\,\%$ of the atoms are transferred. Although this already hints at processes taking place in addition to our model of the dimple trick - where the number of atoms is assumed to be conserved - let us compare the experimental results to the theoretical predictions:

In the left panel of fig. 3.9 we compare the experimentally measured relative temperature increase to the model prediction (blue solid line) and note that the theory overestimates the temperature increase. This discrepancy could have technical reasons (faulty power calibration or bad beam overlap of dimple trap beams resulting in faulty conversion of set value to trap depth) but is (at least partly) explained by the following consideration: The dimple trap is ramped up during $t = 150\,\mathrm{ms}$ where atoms are held at a magnetic field corresponding to a scattering length of $a \approx 640\,a_0$ to allow thermalization. The relevant time scale here - given by the two-

---

[5]imaging the cloud after a very short time of flight to get the real-space density distribution (integrated along the line of sight)

[6]We checked the timescale that we need for adiabatic trap deformations in a separate measurement where we ramped up the dimple trap laser power before ramping it down again, subsequently comparing temperature and atom number
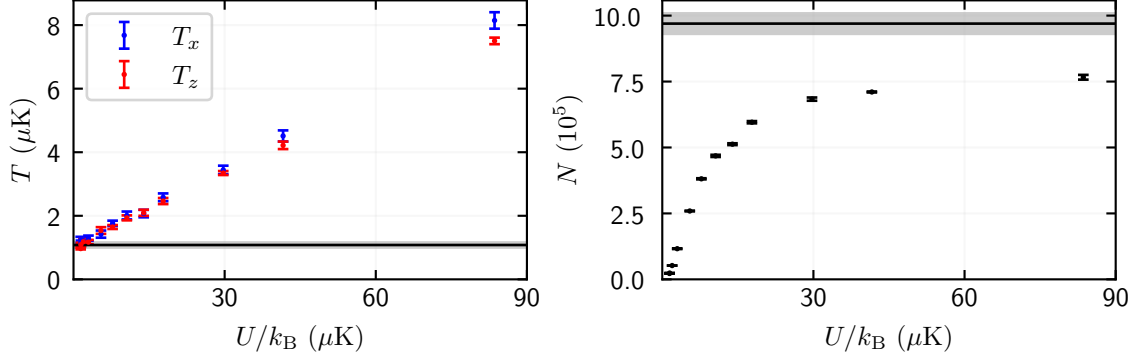
Fig. 3.8: Experimental measurement of the dimple trick. Final temperature (in two perpendicular directions) in the combined traps (left) and final atom number only in the dimple trap (right). The horizontal lines mark the measured initial temperature $T_i = (1.1 \pm 0.1)\,\mu$K and initial number of atoms in the reservoir trap $N_i = (9.7 \pm 0.4) \times 10^5$, respectively. Error bars (and shaded areas) mark the standard deviation of statistical fluctuations between experimental runs. Power calibration and dimple trap beam waist used to plot the results as a function of the dimple trap depth U.

body collision rate - for this scattering length and the measured densities is around $\tau \approx 25\,$ms, which means that the atoms have time to scatter and redistribute their energy. Given that the trapping potential is altered quite drastically (depending on U), it is very likely, that atoms not only thermalize, but some of them also leave the trap, meaning that the sample is evaporatively cooled. This would also explain the transfer efficiency being smaller than one. As it is hard to model the evaporation during the dimple trick (because of the complicated way in which the trapping potential is deformed, see also sec. 3.3), in the following we will correct our theory to (roughly) match the relative temperature increase (orange solid line in fig. 3.9) to check if this is the only deviation between experimental results and model predictions.

The relative density increase in the trap centre $n(0)/n_i(0)$ is shown in the right panel of fig. 3.9. From the experimentally measured atom numbers in the dimple trap only, N, we can calculate the peak density in the trap centre as (eq. (3.7) for a harmonic potential evaluated at $r = 0$)

$$n_{\mathrm{DT}}(0) = N\omega^3 \left(\frac{m}{2\pi k_{\mathrm{B}} T} \right)^{3/2} . \tag{3.10}$$

As this only includes the atoms already transferred to the dimple trap, we need to add the contribution from the RT atoms, i.e. $n(0) = n_{\mathrm{DT}}(0) + n_{\mathrm{RT}}(0)$, to be able to compare to the theory prediction that directly calculates the full density distribution in the combined trapping potential, as described in sec. 3.2.1. The peak density is normalized to the peak density in the RT before the dimple trick
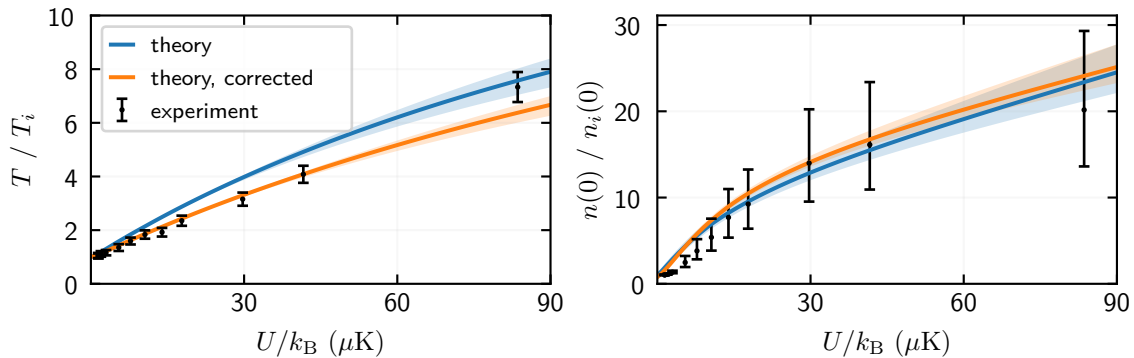
Fig. 3.9: Dimple trick, derived experimental quantities and comparison to theory. Left: relative temperature increase, right: relative peak atom density increase. The markers represent the experimental results derived using the best fit value for the measured RT beam waist. Error bars include statistical fluctuations, see fig. 3.8 as well as the systematic uncertainties in the RT beam waist determination. The theory prediction (with uncertainties from RT beam waist, see fig. 3.7) is shown in blue. A corrected theory curve (see text) - obtained by stretching the prediction as $T(U \cdot 3/4)$ (left panel) and using this together with the measured transfer efficiency ~ 0.8 to calculate the density increase (right panel) - is shown in orange.

$n_i(0) \equiv n_{\mathrm{RT}}(0)$ calculated using eq. (3.10) with $N = N_i$ and $T = T_i$. Both the 'raw' theory prediction and the evaporation-corrected (smaller temperature, see above, and measured transfer efficiency taken into account) match the experimental results reasonably well (error bars include systematic uncertainties stemming mostly from RT beam waist determination as well as statistical fluctuations, see fig. 3.8).

We are now in a position to calculate the experimental PSD gain and compare it to the model prediction, see fig. 3.10. As already the temperature increase is not correctly captured by the model, we cannot hope that the PSD gain is well reproduced, see solid blue line. But when correcting the temperature prediction as described above, the resulting corrected PSD gain curve (solid orange line) reproduces the experimental findings fairly well.

Improvements beyond the current setup

We are now in a position where we can confidently use our model to simulate modifications to the current experimental setup and find parameters where the phase space density is enhanced by more than a factor of ~ 4 which is currently the case. As is already clear from the qualitative two-box model, the ratio of reservoir to dimple volume has to be increased in order to increase the maximally possible PSD gain during the dimple trick. In terms of experimental parameters this leads to two possible approaches: One can either increase the dimple trap frequency (at a certain power, i.e. trap depth) or decrease the initial reservoir trap frequency (again keeping
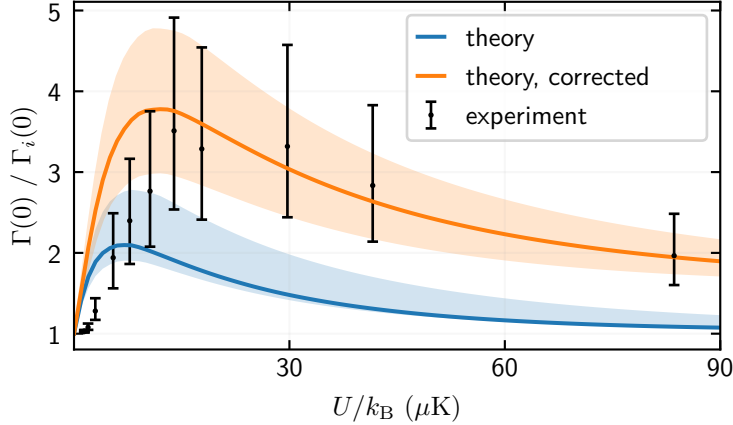
Fig. 3.10: Phase space density increase during the dimple trick, experimental results and comparison to theory. Markers represent derived experimental results and lines show the (corrected) theory prediction, cf. fig. 3.9.

the trap depth unaltered). Keeping in mind that the mean trapping frequency ω (in the harmonic approximation of Gaussian beams) relates to the beam waist w_0 as $\omega \propto 1/w_0^2$ (for fixed laser power) (Grimm et al. 2000), this is consistent with the qualitative arguments above and means that either the dimple beam waist should be decreased or the RT beam waist increased to increase the PSD gain during the dimple trick.

Let us first investigate what happens when the dimple trap beam waist is decreased: The simulations indeed show that the maximally possible PSD gain increases (see left panel of fig. 3.11) and, in principle, this process can be continued until the dimple trap beam waist approaches zero, where the maximal PSD gain practically diverges. This is of course not a realistic scenario because of two factors ultimately limiting us: First, the peak density in ever smaller dimple traps also increases dramatically, which means that a some point three-body losses (see sec. 3.3) will outweigh the increase in PSD gain provided by the optimized dimple trick. Secondly, at this intermediate stage of the experimental sequence, the PSD alone is not the right figure of merit: When decreasing the dimple beam waist, also the number of atoms that can be transferred from RT to DT will decrease. Modelling this by calculating the number of transferred atoms by integrating the final density distribution up to $r_{\mathrm{max,DT}}$, see eq. (3.6), we see that the number of atoms after the dimple trick decreases considerably, see left panel of fig. 3.11. This leads - considering the higher peak density, thus enhanced three-body losses and less efficient evaporation - to the final atom number in the BEC to even decrease with decreasing dimple trap beam waist. For a more in-depth discussion, see Ma et al. 2004.

As decreasing the dimple trap size would probably also have negative consequences for Lithium, let us turn to the other possible scenario, i.e. increasing the RT beam waist. As a larger RT volume would also allow for more atoms to be transferred
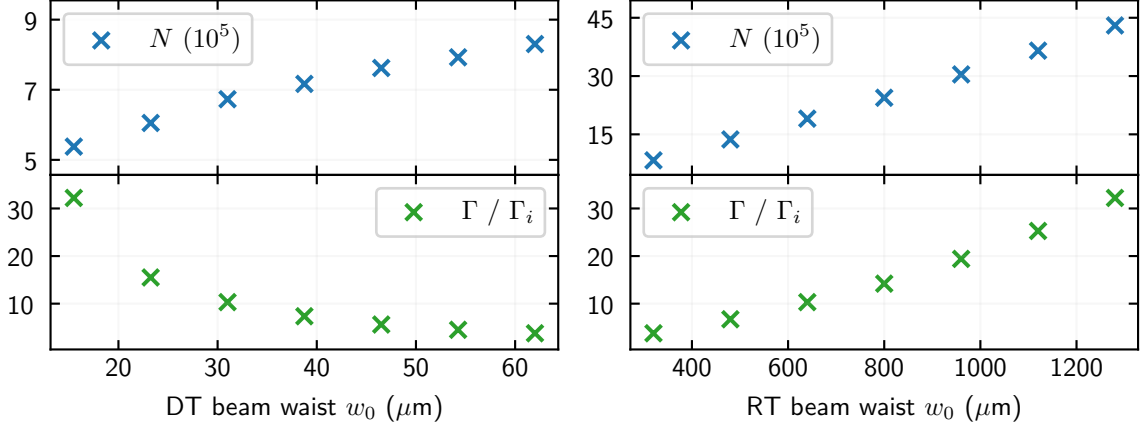
Fig. 3.11: Dimple trick beyond the current experimental setup: Simulations of the number of atoms transferred to the dimple trap (top) and maximal PSD increase during the dimple trick (bottom) for decreasing the dimple trap beam waist (left) or alternatively increasing the RT beam waist (right). The current values for the beam waists of DT and RT are $w_0 = 62\,\mu\text{m}$ and $w_0 = 320\,\mu\text{m}$, respectively. The initial temperature and peak atom density in the RT used here are $T_i = 1.1\,\mu\text{K}$ and $n_i(0) \approx 2.25 \times 10^{11}\,\text{cm}^{-3}$. The temperature after the dimple trick changes less than $2\,\%$ across the simulated regime.

from the dRSC cloud in the first place (see discussion at the beginning of sec. 3.1), we investigate increasing the RT beam waist under the assumption that the initial temperature and peak density in the RT remain unchanged. This assumption implies that also the PSD before the dimple trick remains unaltered and the initial number of atoms in the RT increases. Under these conditions, we see a considerable increase in the number of atoms loaded in the DT after the dimple trick, see right panel of fig. 3.11. This also translates to an increase of the final number of atoms in the BEC, which is a consequence of both better initial conditions for the final evaporation ramps and a larger PSD increase during the dimple trick.

Although the arguments above imply a clear suggestion to increase the RT beam waist, there are some limiting factors that need to be taken into consideration: In order to be able to increase the RT beam waist, both dipole traps need to be separated by a larger distance to avoid Lithium losses during Caesium loading. This implies that at some point in the experimental sequence, atoms need to be moved over a larger distance compared to the current setup, which could be challenging as already now we observe considerable atom losses during the RT move, cf. fig. 3.14. Apart from that, the amount by which the RT beam waist can be increased is technically limited by the available laser power: As at some point of the experimental sequence in the current scheme Caesium needs to be trapped only optically (i.e. without magnetic gradient field), the available laser power has to be sufficient to provide a trap depths of $U/k_\text{B} \approx 10\,\mu\text{K}$ in this situation (assuming temperatures of

the order of $1\,\mu K$), cf. fig. 3.1. Considering that the trap depth U scales with the laser power P and the (mean) beam waist w_0 as $U \propto P/w_0$ this quickly becomes a limiting factor. This constraint could be alleviated e.g. by using a separate dimple trap for Caesium (where Lithium is stored in a different trap during the dimple trick for Caesium) which would make an all-optical trapping of Caesium unnecessary, see the discussion at the end of this chapter.

3.3 Upgraded evaporation efficiency

At this point we almost have all the tools that we need to obtain a good Caesium BEC. What is missing, is an understanding of how to use the different evaporation ramps after the dimple trick in the best way possible. A commonly used proxy, quantifying 'how good' an evaporation works - by comparing the change in phase space density Γ_f/Γ_i to the change in atom number N_f/N_i (on a logarithmic scale) - is the 'evaporation efficiency' defined as

$$\gamma = -\frac{\log\left(\Gamma_f/\Gamma_i\right)}{\log\left(N_f/N_i\right)} \,, \tag{3.11}$$

where the subscripts denote the initial and final values, respectively. In the following, we will first introduce the concepts needed to model the evaporation efficiency in different scenarios before we apply this model to the current Lithium-Caesium experiment.

3.3.1 Conceptual considerations

Olson et al. 2013 introduced a useful model that describes evaporation ramps (in terms of atom number and temperature change) and thus allows for their optimization under some simplifying assumptions: The main assumption is that the evaporation is performed in a deep trap (truncation parameter $\eta \equiv U/k_\mathrm{B}T > 6$, where U denotes the trap depth) such that the truncation of the thermal Boltzmann distribution can be neglected (in three dimensions). The authors also use the harmonic approximation of the trap and introduce the parameter ν that describes the scaling of the mean trap frequency with the trap depth expressed as $\omega \propto U^\nu$. Under these assumptions (and by neglecting interactions), the authors model the effects of evaporation from the trap, externally imposed change in trapping potential as well as one- and three-body losses with the following set of coupled differential equations:

$$\dot{E} = -N\Gamma_\mathrm{ev}(\eta + \kappa)k_\mathrm{B}T + \nu E\frac{\dot{T}}{T} - \Gamma_\mathrm{1B}E - \Gamma_\mathrm{3B}\frac{2}{3}E \,,$$
$$\dot{N} = -\left(\Gamma_\mathrm{ev} + \Gamma_\mathrm{1B} + \Gamma_\mathrm{3B}\right)/N \,. \tag{3.12}$$

Here, the dot denotes a derivate with respect to time and $\kappa \approx (\eta - 5)/(\eta - 4)$ (for a deep, three-dimensional harmonic trap) parametrizes the evaporation process.
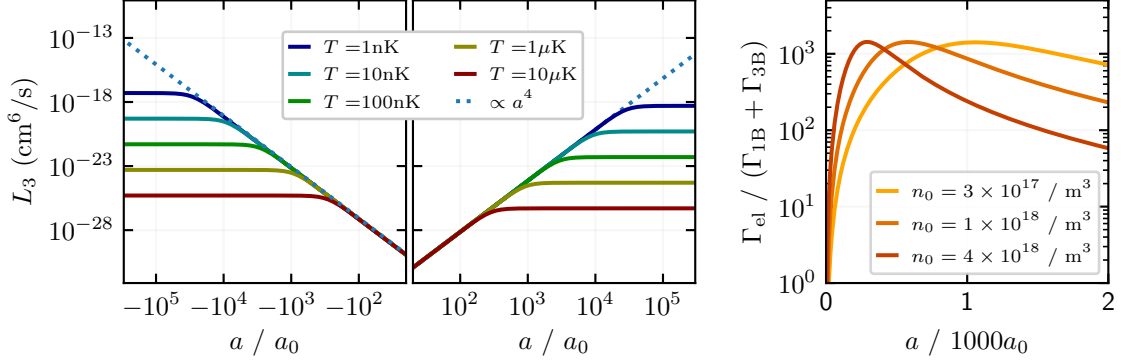
Fig. 3.12: Left panel: Coarse dependence of the three-body loss parameter L_3 for
Caesium on the s-wave scattering length a at different temperatures: The
a^4 dependence is limited by thermal effects ('unitarity limited'). Enhanced
and reduced losses due to interference effects between different recombi-
nation channels are omitted here, for details cf. D'Incao et al. 2004.
Data was calculated by taking the (coarse) functional dependence given
by D'Incao et al. 2004 and fitting it to data taken by Eismann et al.
2016 for ^{133}Cs. Right panel: 'Ratio of good to bad collisions' for different
peak densities varying over the experimentally relevant range, shown for
$T = 100\,\text{nK}$ and $\Gamma_{1B}^{-1} = 60\,\text{s}$.

The evaporation rate Γ_{ev} is approximated as $\Gamma_{ev} \approx (\eta - 4)e^{-\eta}\Gamma_{el}$ with the elastic
collision rate $\Gamma_{el} = n_0\sigma\bar{v}/(2\sqrt{2})$. Here, the elastic cross section (for identical bosons)
$\sigma = 8\pi a^2$ and the average atomic velocity $\bar{v} = 4\sqrt{k_B T/\pi m}$ have been introduced.
For an efficient evaporation one wants to have a high elastic collision rate (which
one could achieve by tuning the magnetic offset field such that the scattering length
a assumes large values) but unfortunately, the scattering length also influences the
three-body losses: The three-body loss rate $\Gamma_{3B} = L_3 n_0^2/(3\sqrt{3})$ is related to the
three-body loss parameter L_3, which follows a universal scaling of $L_3 \propto a^4$ for
$|a| \lesssim \lambda_{dB}/2\pi$, cf. fig. 3.12. Here we neglect changes from this scaling due to the
Efimov effect as discussed in D'Incao et al. 2004.

This shows that the magnetic field, which determines the scattering length a, is
an important parameter that needs to be optimized for an efficient evaporation -
also depending on the density: Note that Γ_{ev} and Γ_{3B} depend on the peak density n_0
(and thus, see eq. (3.10), on the atom number N) which is not explicitly written in
eq. (3.12). Because of this dependence, it is intuitively clear that at lower densities it
can be favourable to use a large scattering length guaranteeing fast thermalization,
whereas at higher densities three-body losses become dominant, thus constraining
the scattering length to smaller values. This is captured in the 'ratio of good to
bad collisions', see right panel of fig. 3.12. However, this simplified picture can
be considerably altered by the presence of three-body loss minima (not included in
fig. 3.12) caused by destructive interference of different loss channels, reducing three-

body losses and thus facilitating the creation of a BEC, cf. Kraemer et al. 2006. The one-body lifetime on the contrary does not depend on density or scattering length and has been measured in our experiment for Caesium in the RT to be $\Gamma_{1B}^{-1} \approx 60\,\mathrm{s}$.

Using that (neglecting interactions) $E = 3Nk_\mathrm{B}T$ eq. (3.12) can be numerically integrated with the initial conditions $E(t = 0) = 3N_ik_\mathrm{B}T_i$ and $N(t = 0) = N_i$, where N_i and T_i are the experimentally determined initial atom number and temperature, respectively.

3.3.2 Application to the Lithium-Caesium experiment

Before we can apply the model introduced above, we have to determine some parameters for our experiment while other parameters can be freely adjusted, which means that they have to be optimized to obtain the desired final BEC with high atom number.

The truncation parameter η can be experimentally controlled by adjusting the ramp 'speed' (depending on the type of ramp, see below, care has to be taken that η stays approximately constant throughout the ramp), i.e. η is a free parameter that will be optimized. The parameter ν in contrast is given by the type of evaporation and has to be determined for each ramp in the experiment: E.g. in a harmonic trap (without any further potentials) and the case of evaporating by lowering the laser power, it holds that $\omega \propto \sqrt{U}$, hence $\nu = 0.5$. For our experiment, however, we want to model two different ramps that are not as easily described: One is forced evaporation by 'tilting' the trapping potential in one direction by lowering (or - in principal - increasing) the magnetic gradient field, cf. fig. 3.1. To find the right value for ν describing this process, we numerically calculate the trapping potentials for different gradient fields and calculate the trap depth U (from the (local) extrema) and the trap frequencies (from a series expansion to second order around the minimum) for different gradient fields and fit $\{A, \nu\}$ to the power law $(\omega/\omega_0) = A\,\omega_0(U/U_0)^\nu$. As the functional dependence in our case is not fully consistent with a power law, this estimation of ν introduces considerable uncertainties. The second evaporation scenario that we are interested in is to 'weaken' the trapping potential by ramping down the laser power. This ramp will be used at the very end of the experimental sequence where both Lithium and Caesium are in the dimple trap and no magnetic gradient fields are present. This case therefore is again different from the ideal harmonic trap weakening which would give $\nu = 0.5$, i.e. we have to perform the same procedure as described above, this time calculating the potential for different laser powers.

As 'tilting' the dimple trap (removing the gradient) depends on the laser power (i.e. trap depth) at which the tilting is performed, the value of ν_tilt varies from $\nu_\mathrm{tilt} = 0.09 \ldots 0.25$ as the trap depth changes as $U/k_\mathrm{B} = 9.5 \ldots 27.5\mu\mathrm{K}$. Similarly, the scenario of 'weakening' the dimple trap (lowering the laser power) depends on the initial laser power (trap depth) and we obtain value of $\nu_\mathrm{weak} = 0.056 \ldots 0.018$ as the trap depth changes as $U/k_\mathrm{B} = 8 \ldots 27.5\mu\mathrm{K}$.

In principle it would be desirable to also model the process of ramping down the

reservoir trap laser power after the dimple trick has been performed. However, it turns out that the trapping frequencies of the combined RT and dimple trap are solely given by the (much narrower) dimple potential (c.f. fig. 3.6), hence the mean trapping frequency does not change when the RT power is ramped down, resulting in $\nu \approx 0$. As in this case the trapping frequency calculated from the harmonic approximation does not adequately describe the underlying trapping potential of the combined traps, we cannot confidently use the evaporation model described above in this situation.

The full sequence that we want to optimize is as follows: After the dimple trick (with levitation), the reservoir trap power is ramped down, whereafter the magnetic gradient field is gradually removed ('tilting') and subsequently the dimple laser power is ramped down ('weakening') to a final trap depth where a BEC is reached. The parameters that we can optimize are: the magnetic field (as a function of time, because also the density changes over time, see above), the truncations parameters η_{tilt} and η_{weak} which determine the ramp times t_{tilt} and t_{weak} as well as the final trap depth. In detail, both ramps are optimized separately: First, η_{tilt} is determined, optimizing the evaporation efficiency γ_{tilt} during the tilting by imposing the final condition that the magnetic gradient field is completely turned off. This also determines the time during which the magnetic gradient field is ramped down, i.e. we can directly calculate the number of atoms and their temperature after this first ramp. Subsequently, η_{weak} is optimized such that γ_{weak} is maximized under the constraint that Bose-Einstein condensation is reached, mathematically expressed by the final PSD reaching $\Gamma = \zeta(3/2)$. This optimization is equivalent to maximizing the number of atoms in the BEC (as the only free parameter in γ_{weak} is the final atom number). As η_{weak} also fixes the time during which the dimple laser power is ramped down, we can now calculate the final atom number in the BEC. We fix the scattering length during each of the ramps and run the optimization for different values to find the optimal magnetic field.

Because of large uncertainties concerning several input parameters (see above) and the accurate determination of trap depths and - frequencies (especially at the end of the sequence where the trap is very shallow) the simulation does not reproduce the experimentally measured evaporation curve adequately. However, the simulations serve as a good starting point for further experimental optimization of the sequence. In fig. 3.13 we present an exemplary sequence and the resulting phase space density (fig. 3.14) that allows for the reliable creation of a Caesium BEC with a few times 10^4 atoms which, however, is not compatible with the intended Lithium mixing in the current setup (see also the discussion at the end of this chapter).

Starting with a MOT load time of $2\,\text{s}$, the first point in fig. 3.14 (on the far right) denotes the cloud after it has been loaded in the shallow ($U/k_{\text{B}} \approx 10\,\mu\text{K}$) RT using the fast switching of magnetic fields (gradient switched to $\sim 31\,\text{G}\,\text{cm}^{-1}$ and offset field to $B \approx 600\,\text{G}$). The first evaporation ramp is performed by changing the offset field to $B = 934\,\text{G}$ (corresponding to a Caesium-Caesium scattering length of $a \approx 840\,a_0$) during $1\,\text{s}$, mostly cancelling the heating effects induced by the magnetic
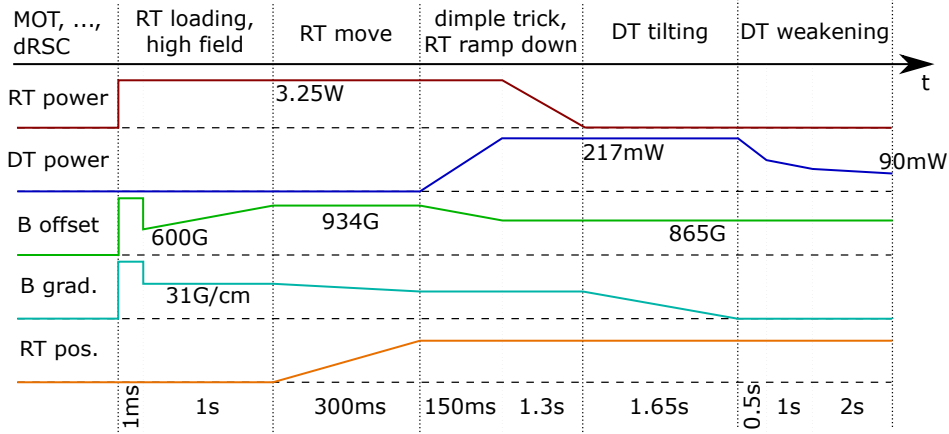
Fig. 3.13: Schematic overview of the optimized experimental sequence in the current setup. Shown are the laser powers of reservoir and dimple trap, the magnetic offset and gradient fields as well as the reservoir trap position as a function of time (not to scale, approximate timings given at the bottom). After dRSC the magnetically levitated RT is loaded facilitated by the fast switching of magnetic fields, it is moved to the centre of the vacuum chamber (magnetic gradient slightly adjusted to maintain the trap depth), the phase space density is adiabatically enhanced and a BEC is reached after forced evaporation by tilting and weakening the DT.

field jump. During the next ramp the RT is moved to the trap centre[7]. The negative slope, i.e. evaporation efficiency, comes from heating and therefore losses during the piezo-mirror driven move which needs to be investigated in the future. After that, the dimple trick is performed by ramping up the DT laser power (during 150 ms) and simultaneously changing the magnetic offset field to $B = 865\,\mathrm{G}$ (corresponding to $a \approx 300\,a_0$) to avoid undue three-body losses because of the higher densities. As it is not possible to calculate the PSD in the combined potential of RT and DT without extensive theoretical modelling, the next data point on fig. 3.14 corresponds to the situation where the RT power has been ramped down (during 1.3 s) and all atoms have been transferred to the DT. This whole process results in an evaporation efficiency of $\gamma \approx 3.2$. During the next ramp, the magnetic gradient field is gradually removed during 1.65 s. This 'tilting' of the dimple trap results in an evaporation efficiency of $\gamma \approx 0.3$, which suggests a very inefficient evaporation. A possible reason for this could be insufficient ergodicity (i.e. not enough scattering) resulting in the one-dimensional tilting (potential only changes in the direction parallel to gravity) being very inefficient. The three subsequent points are measurements during the DT power ramp (total of 3.5 s) where the last point marks the final BEC. The evaporation efficiencies during the DT 'weakening' are $\gamma \approx 2.1, 1.0$ and 3.3, respectively.

---

[7] The move of the reservoir trap is necessary because of the sequential loading of the two separate MOTs for Lithium and Caesium.
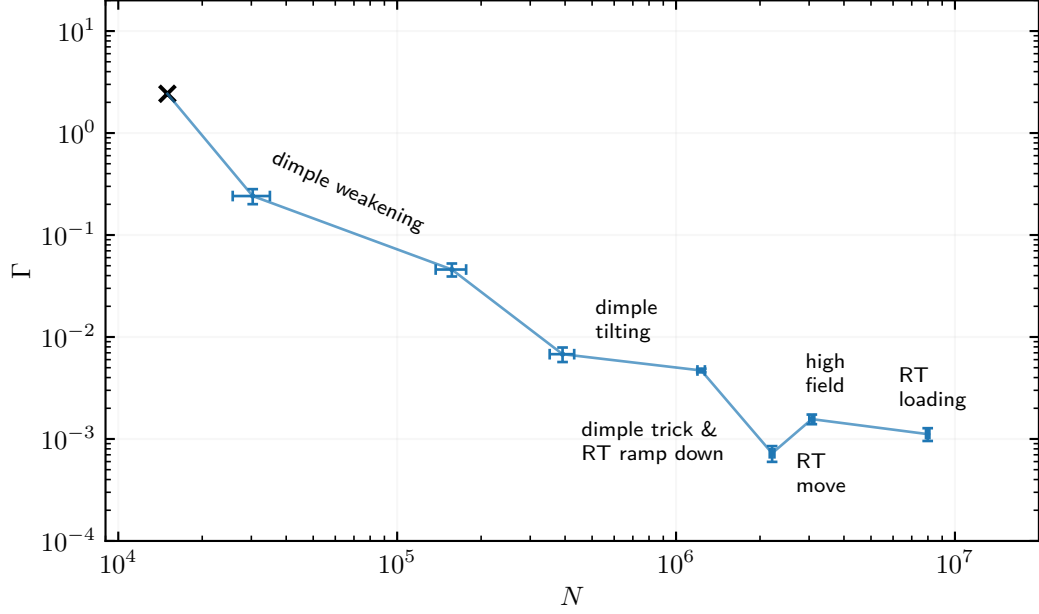
Fig. 3.14: Full evaporation sequence for Caesium with 2 s MOT load time. For details on the sequence, see fig. 3.13 and text. As trapping frequencies and -depths have large uncertainties in the shallow DT, no error bars given on final BEC.

Note, that trap frequencies and -depths strongly depend e.g. on the overlap of the trapping beams in the shallow DT, which is why we cannot confidently give error bars for the last point. This sequence results in a final atom number of $N \approx 3 \times 10^4$ whereof $N_{\mathrm{BEC}} \approx 1.5 \times 10^4$ atoms are condensed. The fraction of condensed atoms (which at the same time highly influences also the total atom number) can be freely adjusted by choosing the final dimple trap depth, e.g. we can produce a sample of $N_{\mathrm{BEC}} \approx 8 \times 10^3$ atoms in a virtually pure BEC, see also fig. 3.15.

In the preceding chapter we discussed various aspects of the creation of a Caesium BEC at high magnetic fields in the current experimental setup and beyond. While some aspects - e.g. the fast switching of the magnetic fields enabling the conceptual improvement of using a shallow, levitated RT for loading Caesium from the dRSC cloud - lead to considerable improvements without major changes to the current setup, the insights regarding the optimization of the dimple trick as well as the forced evaporation ramps suggest considerable changes to the experimental apparatus that are beyond the scope of this work. The findings in sec. 3.2.2 clearly suggest that the reservoir trap volume should be increased. The possible increase in the RT beam waist is conceptually only limited by the size of the Caesium cloud after dRSC but is technically limited by the available laser power.

The minimal laser power needed could be dramatically decreased - making a larger RT beam waist possible - by avoiding only-optical trapping of Caesium: When magnetic gradient fields are used at all times when Caesium is in the RT, considerably
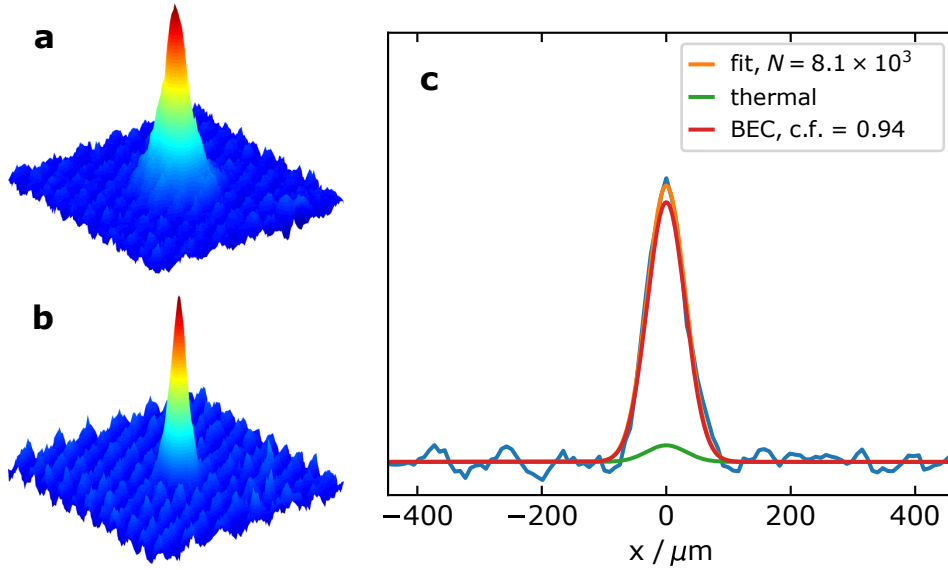
Fig. 3.15: Time of flight (ToF) pictures of final BEC containing information about the momentum distribution. **a** BEC with large thermal part (condensed fraction c.f. $\approx 40\,\%$), **b** almost pure BEC: **c** cut along one direction of the ToF picture in **b** with combined fit of two one-dimensional Gaussian distributions (orange) to determine the total atom number N as well as the thermal (green) and condensed (red) parts. For details on fitting function and calculation of derived parameters, see W. Ketterle et al. 1999.

less power is needed to provide sufficient trap depths. However, this would only be possible if an additional trap was used: E.g. adding a small-volume 'Caesium dimple trap' would allow us to keep Lithium in the DT (we should definitely change its name in that case) at a sufficiently large trap depth such that Caesium could be levitated without too much altering the Lithium trapping potential. In that way, not only could the RT beam waist be increased without the need of a more powerful laser, also the dimple trick for Caesium could be performed with levitation, which is the situation considered in sec. 3.2. Without levitation, simulations suggest that the maximal PSD gain is reduced roughly by a factor of two compared to the levitated case, which can intuitively be understood by the reduced RT volume.

Summing this up, the insights from this chapter result in the following suggestions: Use a shallow, levitated RT, increase the RT volume to a beam waist of at least $600\,\mu\mathrm{m}$ resulting in a PSD gain of 10 to 15 (compared to ~ 4 in the current setup) and use a longer MOT load time for Caesium resulting in a high atom number in the RT prior to the dimple trick. In order to make this compatible with the preparation of Lithium, the Lithium MOT has to be loaded first, the atoms have to be transferred to a separate Lithium trap where they are held at a sufficient distance ($\sim 5\,\mathrm{mm}$) from the Caesium MOT to avoid Lithium losses before both species are combined after the dimple trick for Caesium.

4 Conclusions and Outlook

In the first part of this thesis (chapter 2), the Fermi polaron scenario in a highly mass-imbalanced mixture has been investigated theoretically using the Born-Oppenheimer approximation. The bound state spectrum has been studied as a function of impurity-bath and impurity-impurity interactions as well as the density of the bath in chapter 2.2. In the limit of vanishing fermion density we recovered the well-known Efimov effect including the geometric scaling law as well as deviations from it in the deepest bound Efimov states caused by the impurity-impurity interactions, consistent with previous studies. At finite fermion density, the fermion-mediated impurity-impurity potential develops a repulsive barrier at large radii, suppressing higher-lying bound states and thus cutting off the infinite series of bound states expected from the Efimov scaling law. Furthermore, the Efimov spectrum is altered such that in the presence of a Fermi sea the bound states and resonance positions follow a modified scaling law, now also incorporating the length scale associated with the Fermi sea, the Fermi momentum. This modified scaling law could be numerically confirmed for the case of resonant interactions where again deviations due to the impurity-impurity interaction could be observed for the deepest bound states.

It appears feasible to **experimentally verify our findings on the relation of Efimov and Fermi polaron bound state spectra** in a Lithium-Caesium mixture by virtue of loss measurements, similar to previous Efimov experiments, see e.g. Häfner et al. 2017: Enhanced losses can be measured when the magnetic field is tuned close to a resonance position where the (in-medium) Efimov states merge with the scattering continuum. The shift of these resonance positions with varying fermion density should in principle be detectable. Furthermore, two interspecies Feshbach resonances around $843\,\mathrm{G}$ and $889\,\mathrm{G}$, where the intraspecies Caesium scattering length has negative and positive values, respectively, allow to study the influence of both interactions. We have to point out, however, that the Born-Oppenheimer approximation used throughout our calculations is not able to reproduce the exact results. Quantitative predictions beyond this approximation can be obtained by calculations using the hyperspherical formalism as e.g. described in Naidon and Endo 2017.

Turning to the modified scattering properties of two heavy impurities immersed in a Fermi sea discussed in chapter 2.3, we found **resonances in the induced impurity-impurity scattering length** as well as (for certain parameters) quasibound states that are trapped behind the repulsive barrier of the fermion-mediated potential. Although we cannot hope to experimentally observe these quasibound states directly in a Lithium-Caesium mixture because of the insufficient mass ratio and the associated short lifetimes, they should still show as maxima in the induced

scattering cross section. We expect this enhanced cross section to be detectable in a thermal sample when the mean thermal energy is close to the energy of the quasibound state caught behind the repulsive potential barrier where it should lead to enhanced Caesium losses. To be able to apply our results to a thermal sample of dilute impurities we have to make sure that we are in the right density regime such that all interactions can still be described as pairwise two-body interactions, which is typically the case in ultracold atoms experiments. Still, in our treatment so far we neglected the back-action of the impurities on the Fermi sea (justified by the assumption of zero temperature) which would lead to particle-hole excitations on top of the Fermi sea. This would be very interesting to investigate as it would - at some point - also alter the expected bound state spectrum.

Especially because the whole theory discussion relies on simplifying assumptions (most importantly, Born-Oppenheimer approximation and zero-temperature limit) it would be intriguing to compare the theoretical results to an experiment.

In the second part of this thesis (chapter 3) we focussed on experimental work aiming at the investigation of the polaron scenario, specifically improving the creation of a Caesium Bose-Einstein condensate with high atom numbers in a sequence that at the same time allows for the cooling of Lithium. First, the **efficient loading of the reservoir trap using magnetic levitation facilitated by the fast switching of magnetic fields** was improved as described in sec. 3.1: Decreasing the switching times of both magnetic gradient and offset fields to values $\lesssim 1\,\mathrm{ms}$ allows for the efficient transfer of Caesium atoms to the magnetically levitated reservoir trap. The fast switching also allows to jump to the high magnetic fields close to the Feshbach resonance where the polaron experiments are planned in an efficient way.

Further, special emphasis was put on the **theoretical modelling and experimental verification of the phase space density enhancement by adiabatic trap deformations** in sec. 3.2: We discussed an intuitive model estimating the maximal gain in PSD, subsequently refined the model to make quantitative predictions given experimental parameters, tested these predictions experimentally before using our model to suggest further optimizations regarding the involved traps beyond the current experimental setup. While currently the phase space density is only increased by a factor of ~ 4, we suggest an increase of the reservoir trap volume (entailing major changes to the overall trapping and mixing scheme) aiming at a phase space density increase of 10 to 15 in addition to a considerably increased number of Caesium atoms after the 'dimple trick'.

Lastly, the **evaporation efficiency was optimized** to get an estimate for experimental parameters resulting in the most atoms in the final BEC in sec. 3.3, where in the current experimental setup we achieved a BEC with $\sim 1.5 \times 10^4$ condensed atoms. The simulations concerning the optimization of the different evaporation ramps helped to find experimental parameters for an improved BEC as well as to discover discrepancies with respect to the experiment, hinting at points that should be further investigated and improved in the future. Some theoretical considerations regarding **limits on the final number of Lithium impurities** immersed in the

Caesium BEC are given in appendix A.1 implying that in the current setup it is not possible to image a non-degenerate sample of Lithium impurities at the temperature imposed by the Caesium BEC.

All in all, we were able to gain a detailed understanding of the mechanisms used to create a Caesium BEC with high atom numbers as well as the problems in the current experimental setup preventing us from achieving that goal: Using the new insights we could improve the experimental sequence, see fig. 3.14, and we are confident that with the suggested modifications to the experimental setup, most importantly an increased reservoir trap volume, the goal of a stable Caesium BEC that allows for the mixing with Lithium can be achieved.

As the polaron scenario remains an intriguing research area with still unanswered theoretical questions as well as experimental challenges concerning its investigation, I hope that the work reported in this thesis brings us closer to its understanding. Insights regarding this prototypic effective quantum many-body theory will most likely have an impact on research areas far beyond ultracold quantum gases and could very well - again applied to solid state systems where the idea originally was developed - lead to exciting technological advances.

A Appendix

A.1 Imaging of tightly confined minority atoms

One of the goals of the current experiment is to create an ultracold mixture of ^{6}Li and a ^{133}Cs BEC, preferably in a regime where Lithium is still non-degenerate. At this point Lithium will be confined in an optical tweezer ('micro trap') at a wavelength that does not influence the Caesium trapping potential and therefore can be used to ensure sufficient overlap between the two species, as discussed in detail in Klaus 2019. Given the tight confinement of the micro trap, aiming for a non-degenerate Lithium sample immediately puts a constraint on the maximum number of Lithium atoms at a given temperature. The temperature is considered given because we assume that the two species thermalize, i.e. the Lithium temperature is determined by the (much larger) Caesium BEC.

On the other hand, the number of Lithium atoms still must be able to be measured reliably. To this end, the experiment features resonant absorption imaging for Lithium. In this chapter we are going to investigate the question if (or in what parameter regime) we can reliably image a non-degenerate sample of Lithium in the micro trap. In a first step, we need to determine the minimal atom number (more specifically: the integrated atom column density) that we can resolve with our imaging setup, see sec. A.1.1. Having this limit, we can have a look at the atomic density distributions in the trap at different trapping powers (i.e. -frequencies in harmonic approximation) and also different temperatures to check if the non-degeneracy condition ($T > T_F$, where T_F is the Fermi temperature) for Lithium can still be satisfied, see sec. A.1.2.

A.1.1 Minimally resolvable Lithium atom number

The quantity that directly enables us to determine the detection limit is the signal to noise ratio SNR $= \overline{OD}/\sigma\,[OD]$, in this case regarding the optical depths OD as becomes apparent in the following. Throughout this chapter a bar denotes taking the mean and σ the standard deviation of a given quantity. Ultimately, we need SNR > 1 to be able to reliably detect a signal, i.e. to determine this limit we need the variance of the signal as a function of the signal itself. Conceptionally, there are two ways to obtain this: on the one hand, we can extract the desired quantities from experimental data and on the other hand we can theoretically predict them from a few initial assumptions. Both ways will be shortly presented here, after giving a very brief introduction into absorption imaging.

Absorption imaging

This imaging technique relies on the resonant absorption of laser light by the atomic cloud which is given by the Lambert-Beer law:

$$\frac{dI}{dz} = n\sigma(I)I = -n\sigma_0 \frac{1}{\alpha^* L + I/I_0^{sat}} I \; . \tag{A.1}$$

Here, $I = I(x, y, z)$ is the laser intensity, $n = n(x, y, z)$ is the atomic density, $\sigma(I)$ the effective absorption cross section, $\sigma_0 = 3\lambda^2/2\pi$ the resonant cross section and I_0^{sat} the saturation intensity (in this case for the D_2 line of ^{6}Li). α^* corrects for effects due to polarisation of the imaging light, structure of the excited state and the Zeeman sublevel population of the ground state, see Ockeloen et al. 2010. $L = 1 + 4\,(\Delta/\Gamma)^2$ contains the correction for non-resonant light with Δ being the detuning and Γ the line width of the transition.

Integrating the differential equation above yields (per definition) the optical depth

$$
\begin{aligned}
OD(x,y) &\equiv \sigma_0 \int n(x,y,z)dz = -\int \frac{dI}{I}\left(\alpha^* L + \frac{I}{I_0^{sat}}\right) \\
&= -\alpha^* L \ln\left(\frac{I_{abs} - I_{bac}}{I_{div} - I_{bac}}\right) + \frac{I_{div} - I_{abs}}{I_0^{sat}}
\end{aligned}
\tag{A.2}
$$

where in the last step we integrated from $I_{\mathrm{div}} - I_{\mathrm{bac}}$ to $I_{\mathrm{abs}} - I_{\mathrm{bac}}$ denoting the intensities (at each pixel) taken from three pictures: The division picture, corresponding to the intensity before the light passed the cloud, the absorption picture containing the information about the intensity after the light passed the cloud and the background picture that is subtracted from the other pictures to account for constant background light. Note that in the image processing the last term on the right hand side is neglected because for not too dense clouds $I_{\mathrm{div}} - I_{\mathrm{abs}} \ll I_0^{sat}$. To be able to infer the intensity I from the counts m measured by the CCD camera, we resort to the following linear conversion

$$I = \frac{gd^2\hbar\omega}{qA_{\mathrm{pix}}\tau}\, m \equiv C\, m \; . \tag{A.3}$$

Here, g denotes the camera gain, A_{pix}/d^2 is the effective pixel size in the focal plane, i.e. accounting for the magnification of the imaging system, q is the quantum efficiency, τ is the imaging time and $\hbar\omega$ is the energy of the imaging photons. For the numerical values used in the experiment and in the following calculations, please refer to tab. A.1.

Theoretical model for SNR

The main noise source that we have to model (apart from constant noise originating from read out and dark current of the CCD) is the so-called photon shot noise. By this we mean the noise introduced by the statistical fluctuations of the laser power.

To this end we assume that the laser photons can be treated as independent leading to their number fluctuations following a Poisson distribution.

For the theoretical treatment, let us define $T \equiv m_{\text{out}}/m_{\text{in}}$ and $s \equiv I_{\text{in}}/I_{\text{sat}}$ where $m_{\text{out}} \equiv m_{\text{abs}} - m_{\text{bac}}$ and $m_{\text{in}} \equiv m_{\text{div}} - m_{\text{bac}}$. Then the optical depth reads

$$OD = -L\alpha^{\star} \log T + s(1 - T) . \tag{A.4}$$

Following Horikoshi et al. 2017, by means of standard error propagation and using that for a Poisson distributed random variable x we have $\sigma^2[x] = \bar{x}$ we find its variance to be

$$\sigma^2[OD] = (L\alpha^{\star} + s)^2 \left(\frac{\sigma[m_{\text{in}}]}{\bar{m}_{in}} \right)^2 + (L\alpha^{\star} + sT)^2 \left(\frac{\sigma[m_{\text{out}}]}{\bar{m}_{out}} \right)^2 \tag{A.5}$$

where for the computation it is handy to have T as a function of OD and s which we find by inverting eq. (A.4) to be

$$T(s, OD) = \frac{L\alpha^{\star}}{s} W \left(\frac{s}{L\alpha^{\star}} e^{(s-OD)/L\alpha^{\star}} \right) . \tag{A.6}$$

Here $W(\dots)$ denotes the Lambert W function.

To be able to evaluate eq. (A.5) in a way such that we can compare the results to experimental data, we further need

$$\bar{m}_{\text{in}} = \frac{sN_{\text{sat}}}{g} \qquad \text{and} \qquad \bar{m}_{\text{out}} = \frac{sN_{\text{sat}}T}{g} \tag{A.7}$$

where we introduced the number of photo electrons $N_{\text{sat}}(\tau)$ accumulated in time τ at the saturation intensity I_{sat}. Again, by means of standard error propagation, we find their variances to be

$$\sigma^2[m_{\text{in}}] = \frac{sN_{\text{sat}} + N_{\text{bac}}}{g^2} \qquad \text{and} \qquad \sigma^2[m_{\text{out}}] = \frac{sTN_{\text{sat}} + N_{\text{bac}}}{g^2} . \tag{A.8}$$

Here, $N_{\text{bac}} = g\bar{m}_{\text{bac}}$ (assumed constant, as all images we are going to analyse in sec. A.1.1 are taken with the same exposure time) denotes the photo electrons from the background image.

The complete equation for the signal to noise ratio depending on the intensity relative to the saturation intensity s, exposure time τ and optical depth OD thus reads, cf. Horikoshi et al. 2017

$$\text{SNR} = \frac{OD}{\sqrt{(1 + s)^2 \left(\frac{1}{sN_{\text{sat}}} + \frac{N_{\text{bac}}}{(sN_{\text{sat}})^2} \right) + (1 + sT)^2 \left(\frac{1}{sTN_{\text{sat}}} + \frac{N_{\text{bac}}}{(sTN_{\text{sat}})^2} \right) + \left(\frac{\sigma_{\text{ro}}}{g} \right)^2 + \left(\frac{\sigma_{\text{dc}}\tau}{g} \right)^2}} \tag{A.9}$$
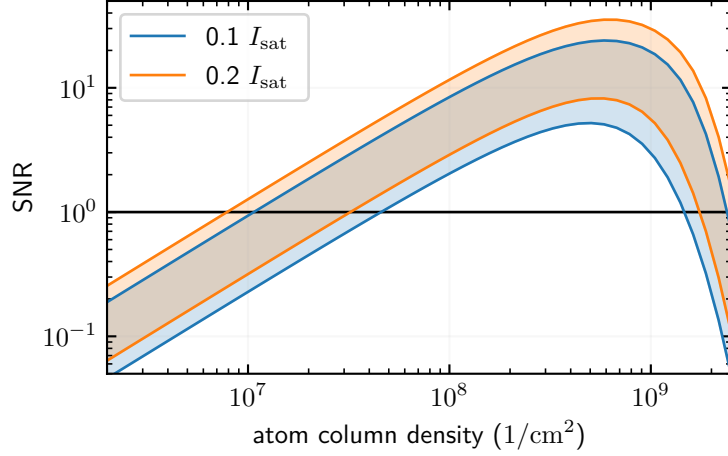
Fig. A.1: Theory prediction for the signal to noise ratio as a function of the atom column density. For each relative saturations $s = 0.1$ and $s = 0.2$ we show two curves corresponding to the exposure times $\tau = 10\mu s$ (lower) and $\tau = 150\mu s$ (upper). For all other parameter values, see tab. A.1. The horizontal line marks the detection limit of SNR > 1.

where we now also included the constant noise originating from readout (σ_{ro}) and dark current (σ_{dc}) which are considered constant here and can thus be added according to Gaussian error propagation to the total noise.

In fig. A.1 we show the results of the theory prediction, using that the optical depth is directly related to the atom column density $n_{2d}(x,y) \equiv \int n(x,y,z)dz$ via the effective cross section, see eq. (A.2).

Extract SNR from measured data

The signal to noise ratio could be extracted straightforwardly from experimental data: Take many pictures of the same experimental procedure (resulting in approximately the same atomic cloud in each run) and calculate mean and standard deviation over the different pictures at each pixel. This should be repeated for different imaging intensities. Unfortunately, at the time of the analysis I did not have access to such a data set or the experiment[1]. Instead, we have to resort to a set of absorption pictures after different hold times, i.e. corresponding to different atom numbers and cloud sizes.

In a first step, we extract the optical depth from the images according to eq. (A.2) (neglecting the second term as described above). Next, we fit a two-dimensional Gaussian function to the OD which in the following defines the signal value at each pixel, cf. left panel of fig. A.2. From this we can also directly calculate the atom column density (at each pixel).

---

[1]thanks, COVID19

symbol	value	explanation / comment	source
g	$2.3\,\mathrm{e^-\,ADU^{-1}}$	gain	Renner 2014
q	$79.1\,\%$	quantum efficiency	Renner 2014
A_{pix}/d^2	$0.0708\,\mathrm{\mu m^2}$	effective pixel size	Filzinger 2018
τ	$80\,\mathrm{\mu s}$	exposure time	
λ	$671\,\mathrm{nm}$	wavelength of imaging laser	Filzinger 2018
L	1	off-resonant scattering correction $(\star)$	Klaus 2019
$\alpha^{\star}$	1	correction factor $(\star)$	Ockeloen et al. 2010
σ_0	$2.15 \times 10^{-13}\,\mathrm{m^2}$	effective cross section	Reinaudi et al. 2007
I_{sat}	$25.4\,\mathrm{W\,m^{-2}}$	saturation intensity	Gehm 2003
N_{bac}	~ 30	background photo electrons (for $\tau = 80\,\mathrm{\mu s}$)	this work
σ_{ro}^2	$12\,\mathrm{e^-\,pix^{-1}}$	read out noise (per pixel)	Eberhard 2016
σ_{dc}^2	$4\,\mathrm{e^-\,s^{-1}\,pix^{-1}}$	dark current noise (per time and pixel)	Eberhard 2016

Table A.1: Typical experimental values used throughout this chapter unless otherwise specified. The values marked with $(\star)$ have not been measured in the experiment thus strictly speaking are assumptions.
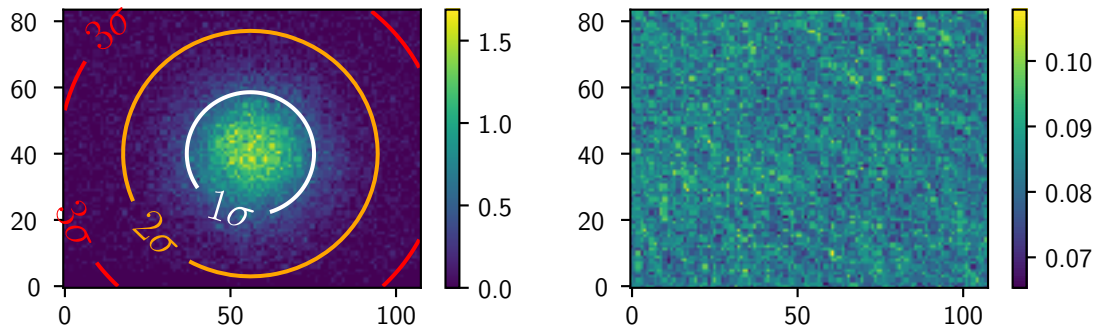
Fig. A.2: Left panel: Typical plot of the optical depth (colour encoded) with contour lines according to a two-dimensional Gaussian fit. The fit indicates a total atom number of $\sim 2.4 \times 10^4$ Lithium atoms. Right panel: noise calculated as the pixel-wise standard deviation of the logarithm of the division pictures. The pixel-wise mean of the division pictures is used to calculate the imaging intensity.
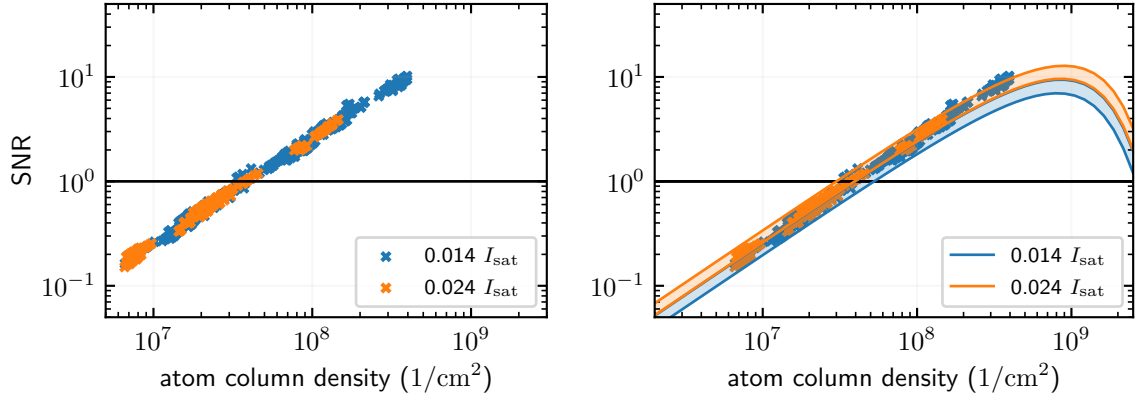
Fig. A.3: Signal to noise ratio extracted form experimental data (left panel). Shown are all SNR values which match the indicated relative intensities within a margin of ± 0.001 (colour encoded). Right panel: Same data overlain with the theory prediction, where the upper and lower curves correspond to exposure times of $\tau = 60\,\mu s$ and $\tau = 100\,\mu s$, respectively (exposure time for experimental data: $\tau = 80\,\mu s$, for all other parameters, see tab. A.1). While the theory prediction and experimental data agree fairly well, the expected dependence on the intensity cannot be verified from the experimental data using the dataset at hand.

To extract the noise from the data set, we take the pixel-wise standard deviation of the logarithm of all division pictures, cf. right panel of fig. A.2. By doing so, we neglect possible fluctuations of the background light as well as fluctuations in atom numbers or their distribution.

From the division pictures we can also extract the relative intensity s by means of eq. (A.3) and the value of the saturation intensity, cf. tab. A.1.

Executing this analysis on a set of eight images (the ones with the highest atom densities, the other images do not add additional information), we calculate the signal to noise ratio depending on the integrated atom column density, see fig. A.3.

A.1.2 Atomic distributions

The detection limit analysis in the previous section sets a limit on the integrated, i.e. two-dimensional, atom distribution. To be able to answer the question whether we can resolve a certain amount of ^{6}Li atoms in a given trap configuration, we need to calculate the atomic distribution for that given scenario.

We consider the following: A small (number and size small compared to Caesium) sample of Lithium atoms is held in the micro trap with adjustable trapping power. The Caesium cloud is trapped in the Dimple trap which according to numerical simulations does not affect the Lithium much in the range where a Caesium BEC can

be produced reliably. Also, gravity (parallel to the z axis in the chosen coordinates) superposes an additional potential. This means that the only free parameter that we can use to control the Lithium atom cloud is the trapping power of the micro trap.

The simulation is structured as follows: In a first step, the complete potential for the Lithium atoms is calculated involving the traps described above as well as gravitational effects. This exact trapping potential is then approximated by a harmonic trapping potential defined by the three trapping frequencies $\omega_{x,y,z}$. Given these, the atomic distributions as well as other derived quantities can be calculated as follows:

The three dimensional atomic distribution for fermions at any temperature T is given by, cf. eq. (3.7)

$$
n(x, y, z) = -\frac{1}{\lambda_{\mathrm{dB}}^3} \mathrm{Li}_{3/2} \left[-\exp \left(\frac{\mu - \frac{m}{2}(\omega_x^2 x^2 + \omega_y^2 y^2 + \omega_z^2 z^2)}{k_B T} \right) \right] , \qquad (A.10)
$$

where $\lambda_{\mathrm{dB}} \equiv \sqrt{2\pi\hbar^2/k_B mT}$ is the thermal de Broglie wavelength, k_B is Boltzmann's constant, m is the mass of ^{6}Li and μ is the chemical potential which is determined by solving the following equation (derived by integrating eq. (A.10) to get the total number of atoms N):

$$
N = -\frac{(k_B T)^3}{\hbar^3 \omega_x \omega_y \omega_z} \mathrm{Li}_3 \left[-\exp \left(\frac{\mu}{k_B T} \right) \right] . \qquad (A.11)
$$

From eq. (A.10) we get the two-dimensional distribution by integrating along the imaging beam which coincides with the z axis:

$$
n_{\mathrm{2d}}(x, y) = -\frac{k_B T}{\hbar \omega_z} \frac{1}{\lambda_{\mathrm{dB}}^2} \mathrm{Li}_2 \left[-\exp \left(\frac{\mu - \frac{m}{2}(\omega_x^2 x^2 + \omega_y^2 y^2)}{k_B T} \right) \right] . \qquad (A.12)
$$

From the previous analysis in Sec. A.1.1 we know that we need at least a peak density $n_{\mathrm{2d}}(0,0) > 6 \times 10^7 \, \mathrm{cm}^{-2}$ to be able to detect the cloud, see gig. A.3. For reliable detection we increase the constraint to $n_{\mathrm{2d}}(0,0) > 1 \times 10^8 \, \mathrm{cm}^{-2}$ for the following discussion. This results in a lower limit for the atom number at given temperature and trapping frequencies (N_{min} in fig. A.4[2]).

As stated earlier, we would like to have a non-degenerate Lithium cloud. To determine the degeneracy we need to compare the experimental temperature T to the Fermi temperature T_F set by the total number of atoms and the trapping frequencies as

$$
k_B T_F = \hbar \sqrt[3]{6N\omega_x \omega_y \omega_z} . \qquad (A.13)
$$

---

[2]for $T = 500\,\mathrm{nK}$ the integrated thermal, i.e. Gaussian, distribution was used to calculate the minimal atom number as $N_{\mathrm{min}} = 2\pi k_B T n_{\mathrm{2d,min}}(0,0)/m\omega_x \omega_y$ in fig. A.4.

I.e. if we impose the non-degeneracy condition $T > T_F$, we get an upper limit on the total number of atoms

$$N \leq N_{\text{max}} \equiv \frac{(k_B T)^3}{6\hbar^3 \omega_x \omega_y \omega_z} \ . \tag{A.14}$$

Both constraints on the total number of atoms are shown in fig. A.4 for different experimental temperatures. We also checked, that if we allow for a degenerate
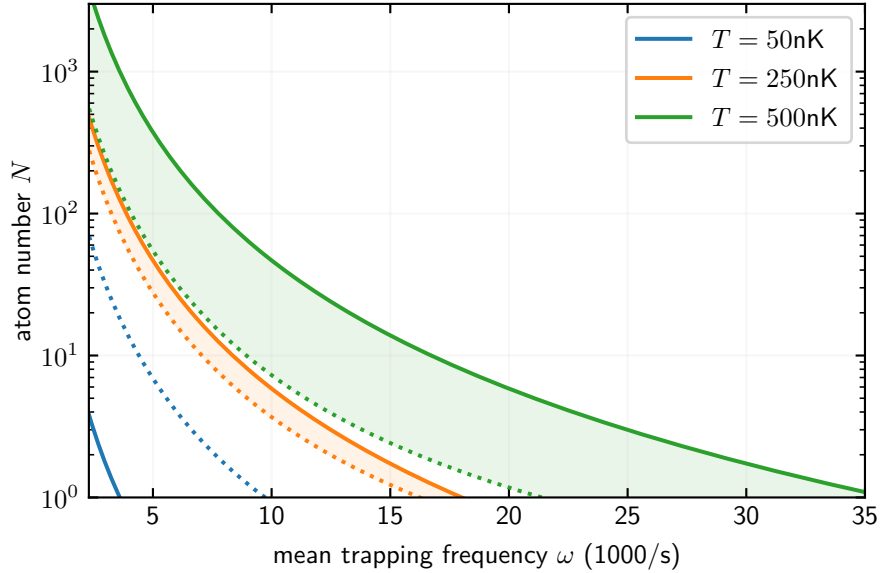
Fig. A.4: Lower (dotted) and upper (solid) limit on the total number of Lithium atoms stemming from detection and non-degeneracy constraints, respectively for different temperatures as a function of the mean trapping frequency. Plotted range corresponds to micro trap laser powers of $P \approx 0.1\,\text{mW}$ to $200\,\text{mW}$. The coloured areas mark the regions where both constraints can be met simultaneously: For $T = 50\,\text{nK}$ there is no micro trap power (determining the trapping frequencies) that satisfies both constraints, whereas for $T \gtrsim 250\,\text{nK}$ both constraints can be met simultaneously.

sample of Lithium atoms, the upper limit of the atom number imposed by the finite trap depth is always met (with a margin of several orders of magnitude).

Concluding, the current setup of the micro trap will not allow the detection of a non-degenerate sample of Lithium atoms at the temperatures imposed by the Caesium BEC as demonstrated in fig. A.4. To meet the requirements of detectability and non-degeneracy, the current beam waist of $\sim 8\,\mu\text{m}$ needs to be increased, either by changing the telescope in the micro trap setup permanently or by introducing an additional variable pin-hole aperture at the adequate position in the micro trap beam which would allow to control the beam waist over a large range.

B List of Figures

C Bibliography

Bloch, Immanuel, Jean Dalibard, and Wilhelm Zwerger (July 2008). "Many-body physics with ultracold gases". In: *Reviews of Modern Physics* 80.3, pp. 885–964. ISSN: 0034-6861. DOI: 10.1103/RevModPhys.80.885. arXiv: 0704.3011.

Braaten, Eric and H.-W. Hammer (June 2006). "Universality in few-body systems with large scattering length". In: *Physics Reports* 428.5-6, pp. 259–390. ISSN: 03701573. DOI: 10.1016/j.physrep.2006.03.001. arXiv: 0410417 [cond-mat].

Calogero, Francesco and Thomas A. Green (June 1968). "Variable Phase Approach to Potential Scattering". In: *American Journal of Physics* 36.6. Ed. by Richard Bellman, pp. 566–567. ISSN: 0002-9505. DOI: 10.1119/1.1975005.

Cetina, Marko, Michael Jag, Rianne S. Lous, Isabella Fritsche, J. T. M. Walraven, Rudolf Grimm, Jesper Levinsen, Meera M. Parish, Richard Schmidt, Michael Knap, and Eugene Demler (Oct. 2016). "Ultrafast many-body interferometry of impurities coupled to a Fermi sea". In: *Science* 354.6308, pp. 96–99. ISSN: 0036-8075. DOI: 10.1126/science.aaf5134. arXiv: 1604.07423.

Chin, Cheng, Rudolf Grimm, Paul Julienne, and Eite Tiesinga (Apr. 2010). "Feshbach resonances in ultracold gases". In: *Reviews of Modern Physics* 82.2, pp. 1225–1286. ISSN: 0034-6861. DOI: 10.1103/RevModPhys.82.1225. arXiv: 0812.1496.

D'Incao, J. P., H. Suno, and B. D. Esry (Sept. 2004). "Limits on Universality in Ultracold Three-Boson Recombination". In: *Physical Review Letters* 93.12, p. 123201. ISSN: 0031-9007. DOI: 10.1103/PhysRevLett.93.123201.

DeSalvo, B. J., Krutik Patel, Geyue Cai, and Cheng Chin (2019). "Observation of fermion-mediated interactions between bosonic atoms". In: *Nature* 568.7750, pp. 61–64. ISSN: 14764687. DOI: 10.1038/s41586-019-1055-0.

Eberhard, Robin (2016). "Imaging of a degenerate gas of ultracold Lithium atoms". Bachelor's thesis. Ruprecht-Karls-Universität Heidelberg, Germany.

Efimov, V. (Dec. 1970). "Energy levels arising from resonant two-body forces in a three-body system". In: *Physics Letters B* 33.8, pp. 563–564. ISSN: 03702693. DOI: 10.1016/0370-2693(70)90349-7.

Eismann, Ulrich, Lev Khaykovich, Sébastien Laurent, Igor Ferrier-Barbut, Benno S. Rem, Andrew T. Grier, Marion Delehaye, Frédéric Chevy, Christophe Salomon, Li-Chung Ha, and Cheng Chin (May 2016). "Universal Loss Dynamics in a Unitary Bose Gas". In: *Physical Review X* 6.2, p. 021025. ISSN: 2160-3308. DOI: 10.1103/PhysRevX.6.021025. arXiv: 1505.04523.

Enss, Tilman, Binh Tran, Michael Rautenberg, Manuel Gerken, Eleonora Lippi, Moritz Drescher, Bing Zhu, Matthias Weidemüller, and Manfred Salmhofer (Dec. 2020). "Scattering of two heavy Fermi polarons: Resonances and quasibound

states". In: *Physical Review A* 102.6, p. 063321. ISSN: 2469-9926. DOI: `10.1103/PhysRevA.102.063321`. arXiv: `2009.03029`.

Feynman, Richard P. (June 1982). "Simulating physics with computers". In: *International Journal of Theoretical Physics* 21.6-7, pp. 467–488. ISSN: 0020-7748. DOI: `10.1007/BF02650179`.

Filzinger, Melina (2018). "Improved manipulation and detection of an ultracold 6Li-133Cs mixture towards the investigation of the Bose polaron". Master's thesis. University of Heidelberg.

Freund, Robert (2019). "Switching polarity of a magnetic gradient field using an H bridge in an ultracold mixture of Lithium and Caesium". Bachelor's thesis. Ruprecht-Karls-Universität Heidelberg, Germany.

Fröhlich, H. (July 1954). "Electrons in lattice fields". In: *Advances in Physics* 3.11, pp. 325–361. ISSN: 0001-8732. DOI: `10.1080/00018735400101213`.

Gehm, Michael Eric (2003). "Preparation of an Optically-Trapped Degenerate Fermi Gas of 6Li: Finding the Route to Degeneracy". Doctoral dissertation. Duke University.

Giannozzi, Paolo (2014). *Numerical methods in quantum mechanics (Lecture Notes)*.

Gribakin, G. F. and V. V. Flambaum (July 1993). "Calculation of the scattering length in atomic collisions using the semiclassical approximation". In: *Physical Review A* 48.1, pp. 546–553. ISSN: 1050-2947. DOI: `10.1103/PhysRevA.48.546`.

Grimm, Rudolf, Matthias Weidemüller, and Yurii B. Ovchinnikov (Feb. 2000). "Optical Dipole Traps for Neutral Atoms". In: *Advances in Atomic, Molecular and Optical Physics*. Vol. 42. C, pp. 95–170. DOI: `10.1016/S1049-250X(08)60186-X`. arXiv: `9902072 [physics]`.

Grusdt, Fabian and Eugene Demler (Oct. 2015). "New theoretical approaches to Bose polarons". In: *Proceedings of the International School of Physics "Enrico Fermi"* 191, pp. 325–411. ISSN: 18798195. DOI: `10.3254/978-1-61499-694-1-325`. arXiv: `1510.04934`.

Häfner, Stephan, Juris Ulmanis, Eva D. Kuhnle, Yujun Wang, Chris H. Greene, and Matthias Weidemüller (June 2017). "Role of the intraspecies scattering length in the Efimov scenario with large mass difference". In: *Physical Review A* 95.6, p. 062708. ISSN: 2469-9926. DOI: `10.1103/PhysRevA.95.062708`. arXiv: `1701.08007`.

Heck, Robert (2012). "All-Optical Formation of an Ultracold Gas of Fermionic Lithium Close to Quantum Degeneracy". Master's thesis. Ruprecht-Karls-Universität Heidelberg, Germany, p. 102.

Horikoshi, Munekazu, Aki Ito, Takuya Ikemachi, Yukihito Aratake, Makoto Kuwata-Gonokami, and Masato Koashi (Oct. 2017). "Appropriate Probe Condition for Absorption Imaging of Ultracold 6 Li Atoms". In: *Journal of the Physical Society of Japan* 86.10, p. 104301. ISSN: 0031-9015. DOI: `10.7566/JPSJ.86.104301`. arXiv: `1608.07152`.

Hu, Ming-Guang, Michael J. Van de Graaff, Dhruv Kedar, John P. Corson, Eric A. Cornell, and Deborah S. Jin (July 2016). "Bose Polarons in the Strongly Interact-

ing Regime". In: *Physical Review Letters* 117.5, p. 055301. ISSN: 0031-9007. DOI: 10.1103/PhysRevLett.117.055301. arXiv: 1605.00729.

Jørgensen, Nils B., Lars Wacker, Kristoffer T. Skalmstang, Meera M. Parish, Jesper Levinsen, Rasmus S. Christensen, Georg M. Bruun, and Jan J. Arlt (July 2016). "Observation of Attractive and Repulsive Polarons in a Bose-Einstein Condensate". In: *Physical Review Letters* 117.5, p. 055302. ISSN: 0031-9007. DOI: 10.1103/PhysRevLett.117.055302. arXiv: 1604.07883.

Ketterle, W., D. S. Durfee, and D. M. Stamper-Kurn (Apr. 1999). "Making, probing and understanding Bose-Einstein condensates". In: *arXiv.* arXiv: 9904034 [cond-mat].

Ketterle, Wolfgang and Martin W. Zwierlein (Jan. 2008). "Making, probing and understanding ultracold Fermi gases". In: *arXiv preprint arXiv:0801.2500.* DOI: 10.1393/ncr/i2008-10033-1. arXiv: 0801.2500.

Klaus, Lauritz (2019). "Design and construction an optical Microtrap to study the Polaron scenario in an ultracold 6Li -133Cs mixture". Master's thesis. Ruprecht-Karls-Universität Heidelberg, Germany.

Kohstall, C., M. Zaccanti, M. Jag, A. Trenkwalder, P. Massignan, G. M. Bruun, F. Schreck, and R. Grimm (May 2012). "Metastability and coherence of repulsive polarons in a strongly interacting Fermi mixture". In: *Nature* 485.7400, pp. 615–618. ISSN: 0028-0836. DOI: 10.1038/nature11065. arXiv: 1112.0020.

Koschorreck, Marco, Daniel Pertot, Enrico Vogt, Bernd Fröhlich, Michael Feld, and Michael Köhl (May 2012). "Attractive and repulsive Fermi polarons in two dimensions". In: *Nature* 485.7400, pp. 619–622. ISSN: 0028-0836. DOI: 10.1038/nature11151. arXiv: 1203.1009.

Kraemer, T., M. Mark, P. Waldburger, J. G. Danzl, C. Chin, B. Engeser, A. D. Lange, K. Pilch, A. Jaakkola, H.-C. Nägerl, and R. Grimm (Mar. 2006). "Evidence for Efimov quantum states in an ultracold gas of caesium atoms". In: *Nature* 440.7082, pp. 315–318. ISSN: 0028-0836. DOI: 10.1038/nature04626. arXiv: 0512394 [cond-mat].

Landau, L D and S I Pekar (1948). "Effective Mass of a Polaron". In: *Zh. Eksp. Teor. Fiz.* 18.5, pp. 417–423. DOI: 10.1016/B978-0-08-010586-4.50072-9.

Lippi, Eleonora, Manuel Gerken, Binh Tran, Stephan Häfner, Marc Repp, Rico Pires, Juris Ulmanis, Bing Zhu, and Matthias Weidemüller (2021). "A platform for the creation and manipulation of an ultracold Fermi-Bose mixture of 6Li and 133Cs atoms". In preparation.

Ma, Zhao-Yuan, Christopher J. Foot, and Simon L. Cornish (Aug. 2004). "Optimized evaporative cooling using a dimple potential: an efficient route to BoseEinstein condensation". In: *Journal of Physics B: Atomic, Molecular and Optical Physics* 37.15, pp. 3187–3195. ISSN: 0953-4075. DOI: 10.1088/0953-4075/37/15/013.

Naidon, Pascal and Shimpei Endo (May 2017). "Efimov physics: a review". In: *Reports on Progress in Physics* 80.5, p. 056001. ISSN: 0034-4885. DOI: 10.1088/1361-6633/aa50e8. arXiv: 1610.09805.

Nascimbène, S., N. Navon, K. J. Jiang, L. Tarruell, M. Teichmann, J. McKeever, F. Chevy, and C. Salomon (Oct. 2009). "Collective Oscillations of an Imbalanced

Fermi Gas: Axial Compression Modes and Polaron Effective Mass". In: *Physical Review Letters* 103.17, p. 170402. ISSN: 0031-9007. DOI: 10.1103/PhysRevLett.103.170402. arXiv: 0907.3032.

Nishida, Yusuke (Jan. 2009). "Casimir interaction among heavy fermions in the BCS-BEC crossover". In: *Physical Review A* 79.1, p. 013629. ISSN: 1050-2947. DOI: 10.1103/PhysRevA.79.013629.

Nygaard, Nicolai Gayle and Nikolaj Thomas Zinner (Feb. 2014). "Efimov three-body states on top of a Fermi sea". In: *New Journal of Physics* 16.2, p. 023026. ISSN: 1367-2630. DOI: 10.1088/1367-2630/16/2/023026. arXiv: 1110.5854.

Ockeloen, C. F., A. F. Tauschinsky, R. J. C. Spreeuw, and S. Whitlock (Dec. 2010). "Detection of small atom numbers through image processing". In: *Physical Review A* 82.6, p. 061606. ISSN: 1050-2947. DOI: 10.1103/PhysRevA.82.061606.

Olson, Abraham J., Robert J. Niffenegger, and Yong P. Chen (May 2013). "Optimizing the efficiency of evaporative cooling in optical dipole traps". In: *Physical Review A* 87.5, p. 053613. ISSN: 1050-2947. DOI: 10.1103/PhysRevA.87.053613. arXiv: 1211.3469.

Ouerdane, H., M. J. Jamieson, D. Vrinceanu, and M. J. Cavagnero (Oct. 2003). "The variable phase method used to calculate and correct scattering lengths". In: *Journal of Physics B: Atomic, Molecular and Optical Physics* 36.19, pp. 4055–4063. ISSN: 0953-4075. DOI: 10.1088/0953-4075/36/19/013. arXiv: 0509155 [physics].

Pillai, Mohandas, Joshua Goglio, and Thad G. Walker (Nov. 2012). "Matrix Numerov method for solving Schrödinger's equation". In: *American Journal of Physics* 80.11, pp. 1017–1019. ISSN: 0002-9505. DOI: 10.1119/1.4748813.

Pinkse, P. W. H., A. Mosk, M. Weidemüller, M. W. Reynolds, T. W. Hijmans, and J. T. M. Walraven (Feb. 1997). "Adiabatically Changing the Phase-Space Density of a Trapped Bose Gas". In: *Physical Review Letters* 78.6, pp. 990–993. ISSN: 0031-9007. DOI: 10.1103/PhysRevLett.78.990.

Pires, Rico (2014). "Observation of Efimov resonances in a mixture with extreme mass imbalance". Doctoral dissertation. Ruprecht-Karls-Universität Heidelberg, Germany.

Pires, Rico, J. Ulmanis, S. Häfner, M. Repp, A. Arias, E. D. Kuhnle, and M. Weidemüller (June 2014). "Observation of Efimov Resonances in a Mixture with Extreme Mass Imbalance". In: *Physical Review Letters* 112.25, p. 250404. ISSN: 0031-9007. DOI: 10.1103/PhysRevLett.112.250404. arXiv: 1403.7246.

Reinaudi, G., T. Lahaye, Z. Wang, and D. Guéry-Odelin (Nov. 2007). "Strong saturation absorption imaging of dense clouds of ultracold atoms". In: *Optics Letters* 32.21, p. 3143. ISSN: 0146-9592. DOI: 10.1364/OL.32.003143. arXiv: 0707.2930.

Renner, Carmen (2014). "Design and characterisation of a dual-wavelength high-resolution imaging system". Wissenschaftliche Arbeit. Ruprecht-Karls-Universität Heidelberg, Germany.

Scelle, R., T. Rentrop, A. Trautmann, T. Schuster, and M. K. Oberthaler (Aug. 2013). "Motional Coherence of Fermions Immersed in a Bose Gas". In: *Physical*

Review Letters 111.7, p. 070401. ISSN: 0031-9007. DOI: `10.1103/PhysRevLett.111.070401`. arXiv: `1306.3308`.

Schirotzek, André, Cheng-Hsun Wu, Ariel Sommer, and Martin W. Zwierlein (June 2009). "Observation of Fermi Polarons in a Tunable Fermi Liquid of Ultracold Atoms". In: *Physical Review Letters* 102.23, p. 230402. ISSN: 0031-9007. DOI: `10.1103/PhysRevLett.102.230402`. arXiv: `0902.3021`.

Schmidt, Richard, Michael Knap, Dmitri A. Ivanov, Jhih-Shih You, Marko Cetina, and Eugene Demler (Feb. 2018). "Universal many-body response of heavy impurities coupled to a Fermi sea: a review of recent progress". In: *Reports on Progress in Physics* 81.2, p. 024401. ISSN: 0034-4885. DOI: `10.1088/1361-6633/aa9593`.

SciPy.org (n.d.). *DOP853*. URL: `https://docs.scipy.org/doc/scipy/reference/generated/scipy.integrate.DOP853.html`.

Stamper-Kurn, D. M., H.-J. Miesner, A. P. Chikkatur, S. Inouye, J. Stenger, and W. Ketterle (Sept. 1998). "Reversible Formation of a Bose-Einstein Condensate". In: *Physical Review Letters* 81.11, pp. 2194–2197. ISSN: 0031-9007. DOI: `10.1103/PhysRevLett.81.2194`. arXiv: `9805022 [cond-mat]`.

Sun, Mingyuan and Xiaoling Cui (June 2019). "Efimov physics in the presence of a Fermi sea". In: *Physical Review A* 99.6, p. 060701. ISSN: 2469-9926. DOI: `10.1103/PhysRevA.99.060701`. arXiv: `1903.09751`.

Sun, Mingyuan, Hui Zhai, and Xiaoling Cui (July 2017). "Visualizing the Efimov Correlation in Bose Polarons". In: *Physical Review Letters* 119.1, p. 013401. ISSN: 0031-9007. DOI: `10.1103/PhysRevLett.119.013401`.

Tran, Binh, Michael Rautenberg, Manuel Gerken, Eleonora Lippi, Bing Zhu, Juris Ulmanis, Moritz Drescher, Manfred Salmhofer, Tilman Enss, and Matthias Weidemüller (Apr. 2021). "Fermions Meet Two Bosonsthe Heteronuclear Efimov Effect Revisited". In: *Brazilian Journal of Physics* 51.2, pp. 316–322. ISSN: 0103-9733. DOI: `10.1007/s13538-020-00811-5`. arXiv: `2009.13221`.

Ulmanis, Juris (2017). *Heteronuclear Efimov Scenario in Ultracold Quantum Gases*. Springer Theses. Cham: Springer International Publishing. ISBN: 978-3-319-51861-9. DOI: `10.1007/978-3-319-51862-6`.

Ulmanis, Juris, Stephan Häfner, Rico Pires, Eva D. Kuhnle, Yujun Wang, Chris H. Greene, and Matthias Weidemüller (Oct. 2016). "Heteronuclear Efimov Scenario with Positive Intraspecies Scattering Length". In: *Physical Review Letters* 117.15, p. 153201. ISSN: 0031-9007. DOI: `10.1103/PhysRevLett.117.153201`. arXiv: `1608.01477`.

Wang, Yujun, Jia Wang, J. P. D'Incao, and Chris H. Greene (Dec. 2012). "Universal Three-Body Parameter in Heteronuclear Atomic Systems". In: *Physical Review Letters* 109.24, p. 243201. ISSN: 0031-9007. DOI: `10.1103/PhysRevLett.109.243201`. arXiv: `1207.6439`.

Yan, Zoe Z., Yiqi Ni, Carsten Robens, and Martin W. Zwierlein (Apr. 2020). "Bose polarons near quantum criticality". In: *Science* 368.6487, pp. 190–194. ISSN: 0036-8075. DOI: `10.1126/science.aax5850`. arXiv: `1904.02685`.

Acknowledgements

Statement of Authorship

I herewith declare that this thesis was solely composed by myself and that it constitutes my own work unless otherwise acknowledged in the text. I confirm that any quotes, arguments or concepts developed by another author and all sources of information are referenced throughout the thesis. This work has not been accepted in any previous application for a degree.

Heidelberg, February 28, 2021